A Study of Cirrus Ice Particle Size Distribution Using TC4 Observations

LIN TIAN,* GERALD M. HEYMSFIELD,+ ANDREW J. HEYMSFIELD,# AARON BANSEMER,#
LIHUA LI,+ CYNTHIA H. TWOHY,@ AND RAMESH C. SRIVASTAVA*,&

* *Goddard Earth Science and Technology Center, University of Maryland, Baltimore County, Baltimore, Maryland*
+ *NASA Goddard Space Flight Center, Greenbelt, Maryland*
# *National Center for Atmospheric Research, Boulder, Colorado*
@ *University of Oregon, Eugene, Oregon*
& *Department of the Geophysical Sciences, University of Chicago, Chicago, Illinois*

(Manuscript received 23 February 2009, in final form 2 June 2009)

ABSTRACT

An analysis of two days of in situ observations of ice particle size spectra, in convectively generated cirrus, obtained during NASA's Tropical Composition, Cloud, and Climate Coupling (TC4) mission is presented. The observed spectra are examined for their fit to the exponential, gamma, and lognormal function distributions. Characteristic particle size and concentration density scales are determined using two (for the exponential) or three (for the gamma and lognormal functions) moments of the spectra. It is shown that transformed exponential, gamma, and lognormal distributions should collapse onto standard curves. An examination of the transformed spectra, and of deviations of the transformed spectra from the standard curves, shows that the lognormal function provides a better fit to the observed spectra.

1. Introduction

In recent years, there has been considerable interest in the study of the size distribution of ice particles in clouds. Study of the ice particle size distribution (IPSD) is important for at least three reasons. First, it is of intrinsic value for validating and advancing our understanding of the microphysical processes underlying the production and evolution of the ice particles. Second, it is of importance in climate studies because the IPSD and the particle shapes affect the radiation balance of the earth–atmosphere system. Finally, knowledge of the IPSD helps in remote sensing of ice water content (IWC), mean size of ice particles, and other parameters of the IPSD, which affect the earth's climate. Indeed, climate studies have been the main impetus for the recent explosion in the study of ice in clouds.

A number of authors have presented in-depth analyses of extensive in situ measurements of IPSDs (e.g., Heymsfield and Platt 1984; Brown and Francis 1995; Heymsfield et al. 2002; Delanoë et al. 2005; Field et al. 2005, 2007; Tinel et al. 2005). One objective of these studies has been to find a few parameters that are sufficient to describe an entire IPSD. For this purpose, many authors have normalized the particle size and concentration using one or two moments of the IPSD. Plots of normalized concentration against normalized particle size, called normalized spectra, for a population of IPSDs, have been found to cluster around a ''universal'' curve or distribution, irrespective of the values of the moments of individual IPSDs. Knowledge of the universal distribution and the moments, used for the normalization, are then sufficient to recover an entire distribution and calculate its properties. Field et al. (2005, 2007) presented an analysis of this type; they found that the universal distribution could be represented by the sum of an exponential and a gamma function.

In this paper, we present an analysis of IPSDs observed in tropical cirrus during the National Aeronautics and Space Administration's (NASA's) Tropical Composition, Cloud, and Climate Coupling (TC4) mission (see http://www.espo.nasa.gov/tc4/). Our aim is to find the best functional representation of the observed IPSDs. In section 2, we present an overview of the data and their meteorological context. In section 3, we present methods for transforming IPSDs that can collapse the exponential, gamma, and lognormal function distributions onto curves

Corresponding author address: Lin Tian, NASA Goddard Space Flight Center, Code 613.1, Greenbelt, MD 20771.
E-mail: tian@agnes.gsfc.nasa.gov

DOI: 10.1175/2009JAS3114.1

whose equations can be predicted in advance. In section 4, we present results of applying the transformations to our data. We shall find that the lognormal function provides a better fit to our data than either the exponential or the gamma function. In section 5, we compare our method of transforming the IPSD to methods of normalizing the IPSD that have been presented in the literature. We conclude with a summary and conclusions in section 6.

2. Data used in this study

The IPSD data used in this study were taken during NASA's TC4 mission designed to investigate the physical properties of convectively generated cirrus clouds. It took place from July 17 to 8 August 2007 near Costa Rica. During TC4, two airborne radars—the ER-2 Doppler radar (EDOP; Heymsfield et al. 1996) operating at 9.7 GHz (3.1 cm wavelength) and the cloud radar system (CRS; Li et al. 2004) operating at 94 GHz (3.2 mm wavelength) onboard the NASA ER-2 aircraft—flew over a number of convectively generated cirrus while an instrumented NASA DC-8 aircraft flew under the ER-2, inside the cirrus cloud, providing coincident in situ microphysical measurements.

The ice particle sizes were provided by a 2D cloud imaging probe (CIP) and a precipitation imaging probe (PIP). CIP measured particle size from about 50–100 microns to above 1 mm (Baumgardner et al. 2002), and PIP measured particles size from about 100 microns to 6.2 mm. Particles were binned into 35 size ranges with bin widths of 50–100 μm for CIP and 0.2 to 0.5 mm for PIP. The ice particles are generally irregular in shape. The particle size is specified by the true maximum dimension of the 2D projected image. This dimension will be referred to as the particle diameter. Comparisons with a 2D-S (stereo) probe with higher resolution and a lower detection threshold suggest that the concentrations from CIP are reliable only down to 100 μm. Therefore, in our analysis we discarded particle sizes below 100 μm. The particle probe data are averaged over 5-s intervals or about a 1.0-km horizontal path.

In addition to the particle probes, the DC-8 carried a counterflow virtual impactor (CVI) probe (Twohy et al. 1997), which provided direct in situ measurements of ice water content, coincident with the IPSD measurements. The minimum particle size sensed by the CVI is about 8 μm. The uncertainty in the IWC is about 11% at 0.2 g m^{-3}, increasing with decreasing IWC to 23% at an IWC of 0.01 g m^{-3}.

We selected for analysis two cases that had the best coordination between ER-2 and DC-8 flights so that the radar and microphysical measurements were collocated in space and time.

a. Case 1: 31 July 2007

On this day, the ER-2 and DC-8 made coordinated flights along northwest–southeast legs oriented over San Jose and extending to near the Panamanian border. Figure 1 shows the Geostationary Operational Environmental Satellite (GOES) IR satellite image with ER-2 and DC-8 flight tracks superimposed. The flight legs followed the developing anvil cirrus formed by a cell located off the Pacific coast at about 9.5°N, 85°W. Parallel racetracks (24 km offset) drifted to the west as the anvil evolved. At about 1545 UTC, the ER-2 moved further west to over fly strong developing cells with active lightning at about 9°N, 84.2°W (at about 1600 UTC), followed by an orthogonal run.

Figures 2a and 2b show the reflectivity measured by the EDOP (X-band, 3.1 cm wavelength, 10 GHz) and the CRS (W-band, 3.2 mm wavelength, 94 GHz) radars, along with the DC-8 flight line between 1400 and 1409 UTC. The cirrus cloud sampled by the ER-2 and DC-8 is associated with a developing convective cell. The minimum detectable reflectivity is about -5 dBZ for EDOP and -28 dBZ for CRS at range of 15 km from ER-2. Such high sensitivities make EDOP and CRS ideal for studying this kind of cirrus cloud. For this case, the X-band reflectivities range between -5 and 15 dBZ and the W-band reflectivities range between -28 and 8 dBZ. At relative distances less than about 150 km, near the cloud top, the reflectivity at both radar frequencies is about the same, an indication that the ice particles are Rayleigh scatterers. The air temperature at DC-8 flight level was about -40°C. The time difference between the radar and the in situ microphysical measurements was less than 45 s and the maximum horizontal distance between ER-2 and DC-8 was less than 0.7 km. The IWC measured by CVI is shown in Fig. 2c. Approximately half the CVI data are missing during this flight because of a valve that periodically opened the system to aircraft cabin air; however, the remaining data were unaffected. The black line shows the IWC calculated from the measured IPSDs, using the Brown and Francis (1995) mass–diameter relationship ($m = 2.939 \times 10^{-3} D^{1.9}$, with D in centimeters and m in grams). Other relations have been suggested (see, e.g., Heymsfield et al. 2004), but the focus of this paper is on the ice particle size distribution. We include the IWC calculated from ice spectra here only for illustration purposes. There is good agreement between the IWC measured by CVI and that calculated from the measured IPSDs. The vertical lines on Fig. 2c indicate four selected locations for which IPSDs will be presented in section 4a.

b. Case 2: 8 August 2007

This is a case of decaying convection with light stratiform rain. The GOES IR image (Fig. 3) shows scattered

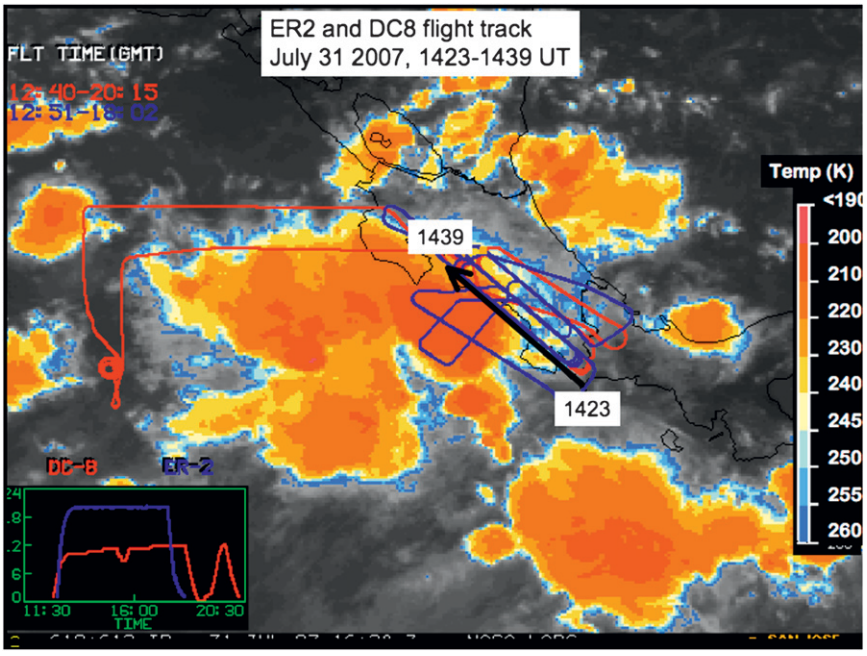

FIG. 1. GOES IR images with ER-2 (blue) and DC-8 (red) flight tracks superimposed. The thick black line shows the flight track for the case 1, 1423–1439 UTC 31 Jul 2007.

convective cells. Figures 4a and 4b show the reflectivities measured by EDOP and CRS radars during 1400–1409 UTC. The cloud sampled is along the edge of a decaying convection with light precipitation. Both X-band and W-band reflectivities are much higher compared to case 1. At the DC-8 flight level, most of the cloud is below the detection level of EDOP. Figure 4c shows that the IWC calculated from IPSD is about 10% to 25% higher than that measured by CVI.

3. Transformation of particle size distributions: Equations

a. *Functional representation of particle size distribution*

Our aim is to represent the observed IPSDs by an analytical expression with a few parameters. In the past, the general exponential, the gamma, and the lognormal functions have been used to describe IPSDs and raindrop size distributions (RSDs). These functions are

$$^{(E)}N_D = {}^{(E)}N_0 \exp(-{}^{(E)}\Lambda D) \text{ (general exponential)}, \quad (1)$$

$$^{(G)}N_D = {}^{(G)}N_0 D^{\mu} \exp(-{}^{(G)}\Lambda D) \text{ (gamma)}, \quad \text{and} \quad (2)$$

$$^{(L)}N_D = \frac{N_T}{\sqrt{2\pi}s}\frac{1}{D}\exp\left[-\frac{\ln^2(D/{}^{(L)}D_*)}{2s^2}\right] \text{ (lognormal)}. \quad (3)$$

In the above, $^{()}N_D dD$ represents the concentration (m^{-3}) of particles with maximum diameter D to $D + dD$ and the left superscripts E, G, and L signify exponential, gamma, and lognormal functions, respectively. The general exponential has two free parameters $^{(E)}N_0$ and $^{(E)}\Lambda$. It has been widely used to represent raindrop and snow size distributions (e.g., Gunn and Marshall 1958; Waldvogel 1974). The Marshall–Palmer distribution (Marshall and Palmer 1948) is a special case of the general exponential distribution with only one free parameter, namely $^{(E)}\Lambda$, with $^{(E)}N_0$ being fixed at 0.08 cm^{-4}. The three-parameter ($^{(G)}N_0$, μ, $^{(G)}\Lambda$) gamma function has been extensively used in the study of raindrop size distributions (e.g., Ulbrich 1983). It has also been used in the analysis of IPSDs. The lognormal distribution also has three parameters (N_T, $^{(L)}D_*$, s). It has been used to describe aerosol size distributions (Seinfeld and Pandis 1998, chapter 7) and occasionally raindrop size distributions (Feingold and Levin 1986). Another function, the modified gamma function, which has four parameters, has occasionally been used to represent IPSDs (Delanoë et al. 2005).

b. *Transformation of particle size distribution*

We shall answer the question: Of the distributions (1), (2), and (3), which one best fits the observed IPSDs? For this purpose, we can perform appropriate regressions to determine the "best" fits to the observed IPSDs. For example, for distribution (1), we could use linear least

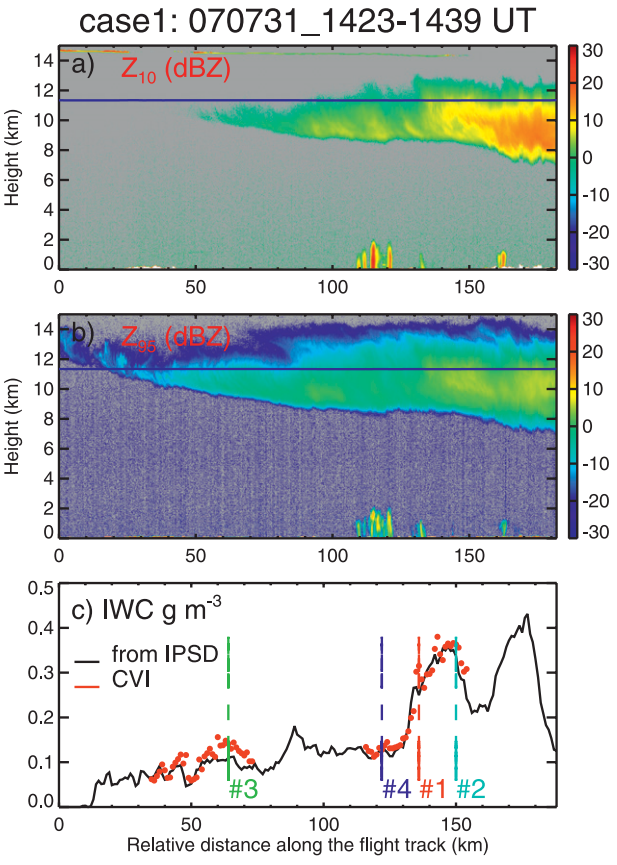

FIG. 2. Observed radar reflectivity by (a) EDOP (X-band) and (b) CRS (W-band) radars for case 1, 31 July 2007. The horizontal line at about 11-km height shows the DC-8 flight line. (c) IWC measured by CVI instrument on DC-8 (red) and IWC estimated from measured IPSDs using the Brown-Francis (1995) mass–diameter relationship (black). The vertical lines indicate the four selected locations for which IPSDs are plotted in Fig. 5a.

squares regression of $\ln N_D$ versus D to determine the best values of ${}^{(E)}N_0$ and ${}^{(E)}\Lambda$; for lognormal distribution (3), we could use second-degree polynomial fit of $\ln N_D$ versus $\ln D$ to determine the best fit. Then we could examine the differences between the observed and fitted distributions to determine which function provides a better description of the data.

Here, instead of performing regressions, we devise transformations of the particle size and concentration such that the transformed distribution takes on a form independent of the values of the parameters of the distribution. For example, for the general exponential distribution (1), we present transformations of the size and concentration such that all exponential distributions, irrespective of the values of ${}^{(E)}N_0$ and ${}^{(E)}\Lambda$, collapse on to a curve whose equation is predicted in advance. We give below the transformations for each of the three functions.

1) EXPONENTIAL DISTRIBUTION

For the exponential distribution, we use ${}^{(E)}N_D/{}^{(E)}N_0$ and ${}^{(E)}\Lambda D$ as the transformed concentration and size variables. We can estimate ${}^{(E)}\Lambda$ and ${}^{(E)}N_0$ using any two moments of the distribution. Here we use the second and fourth moments because they are closely related to the IWC and the radar reflectivity for Rayleigh scattering. This is because many observational studies have found a power-law relationship between particle mass and diameter, $m = aD^b$, with the exponent b ranging between about 1.8 and 2.2 (e.g., Locatelli and Hobbs 1974; Brown and Francis 1995; Heymsfield et al. 2004). With $b = 1.8$ to 2.2, the second moment is closely proportional to the ice water content. Further, in the Rayleigh regime, the backscattering cross section is proportional to the square of the particle mass; therefore, the radar reflectivity is closely proportional to the fourth moment of the IPSD.

The second and fourth moments of the exponential distribution are given by

$$ {}^{(E)}M_2 = \int_0^\infty D^2({}^{(E)}N_D)\,dD = \frac{2!({}^{(E)}N_0)}{{}^{(E)}\Lambda^3}, \tag{4}$$

$$ {}^{(E)}M_4 = \int_0^\infty D^4({}^{(E)}N_D)\,dD = \frac{4!({}^{(E)}N_0)}{{}^{(E)}\Lambda^5}. \tag{5}$$

From the above, we can derive the following:

$$ {}^{(E)}D_* = \frac{1}{{}^{(E)}\Lambda} = \sqrt{\frac{({}^{(E)}M_4/{}^{(E)}M_2)}{12}}, \tag{6}$$

$$ {}^{(E)}N_0 = \frac{({}^{(E)}M_2/{}^{(E)}D_*^3)}{2}. \tag{7}$$

In terms of ${}^{(E)}D_*$ and ${}^{(E)}N_0$, the exponential distribution becomes

$$ \frac{{}^{(E)}N_D}{{}^{(E)}N_0} = \exp\left(-\frac{D}{{}^{(E)}D_*}\right). \tag{8}$$

For an observed IPSD, the moments and the characteristic scales, ${}^{(E)}D_*$ and ${}^{(E)}N_0$, can be estimated using the following equations:

$$ \hat{M}_2 = \sum(N_k \Delta D_k)D_k^2, \quad \hat{M}_4 = \sum(N_k \Delta D_k)D_k^4, \tag{9}$$

$$ {}^{(E)}\hat{D}_* = \sqrt{\frac{(\hat{M}_4/\hat{M}_2)}{12}}, \quad {}^{(E)}\hat{N}_0 = \frac{(\hat{M}_2/{}^{(E)}\hat{D}_*^3)}{2}. \tag{10}$$

Here the hat on top of a symbol denotes an estimate from measurements; N_k is the measured concentration density in the kth size category; ΔD_k is the width of that size category and D_k is its central diameter. Using

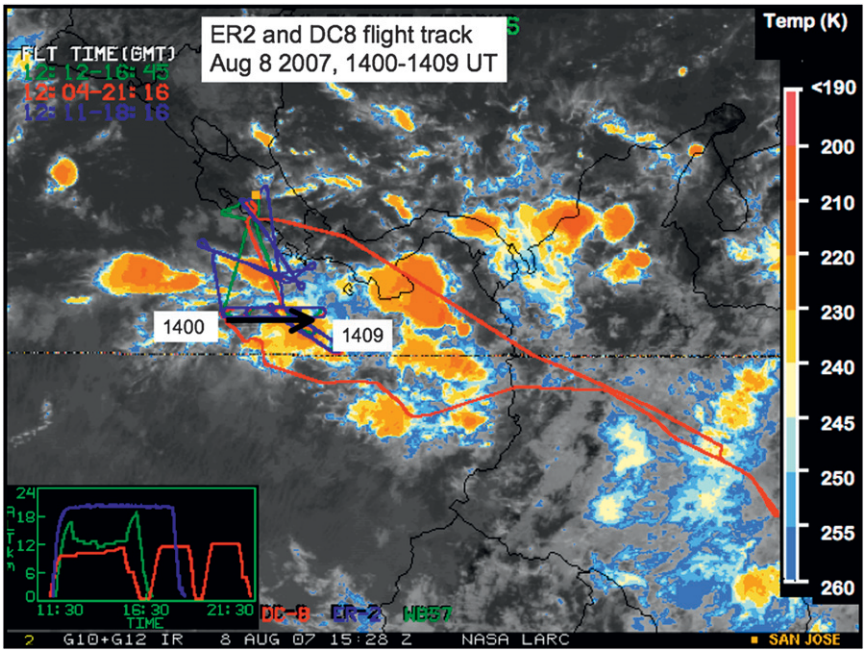

FIG. 3. GOES IR image with ER-2 (blue) and DC-8 (red) flight tracks superimposed. The thick black line shows the flight track for case 2, 1400–1409 UTC 8 Aug 2007.

$y = N_D/{}^{(E)}\hat{N}_0$ and $x = D/{}^{(E)}\hat{D}_*$ as the transformed concentration and size, respectively, where N_D is the observed concentration density, exponential IPSDs should collapse onto an exponential curve $y = \exp(-x)$, irrespective of the values of their parameters.

This scaling is essentially similar to that used by Sekhon and Srivastava (1971) and other two-moment normalizations (e.g., Willis 1984); this is further discussed in section 5, where we compare our transformations with other normalization methods discussed in the literature.

2) GAMMA DISTRIBUTION

The gamma function distribution becomes independent of its parameters if ${}^{(G)}\Lambda D$ and ${}^{(G)}N_D/({}^{(G)}N_0 D^{\mu})$ are used as the size and concentration variables. We use the first, second, and fourth moments to determine the three parameters, ${}^{(G)}\Lambda$, μ, and ${}^{(G)}N_0$. The reason for using the second and fourth moments has been explained above. The first moment has microphysical applications, for example, in the calculation of diffusional growth. The nth moment of the gamma distribution is given by

$$
\begin{aligned}
{}^{(G)}M_n &= \int_0^{\infty} D^n({}^{(G)}N_D)\, dD \\
&= \frac{({}^{(G)}N_0)\Gamma(n+\mu+1)}{{}^{(G)}\Lambda^{n+\mu+1}}, \quad n > -(\mu+1). \qquad (11)
\end{aligned}
$$

Using the above equation with $n = 1$, 2, and 4, we can derive the following:

$$
{}^{(G)}D_* = \frac{1}{{}^{(G)}\Lambda} = \sqrt{\frac{({}^{(G)}M_2/{}^{(G)}M_1)^2}{16} + \frac{({}^{(G)}M_4/{}^{(G)}M_2)}{2}} - \left(\frac{3}{4}\right)\left(\frac{{}^{(G)}M_2}{{}^{(G)}M_1}\right), \qquad (12)
$$

$$
\mu = \frac{{}^{(G)}M_2}{{}^{(G)}M_1}\frac{1}{{}^{(G)}D_*} - 2, \quad \text{and} \qquad (13)
$$

$$
{}^{(G)}N_0 = \frac{[{}^{(G)}M_1/({}^{(G)}D_*^{(\mu+2)})]}{\Gamma(\mu+2)}. \qquad (14)
$$

Using y and x as the transformed concentration and size variables, where

$$
y = \frac{{}^{(G)}N_D}{({}^{(G)}N_0 D^{\mu})} \quad \text{and} \quad x = \frac{D}{{}^{(G)}D_*}, \qquad (15)
$$

any gamma function distribution transforms to

$$
y = \exp(-x), \qquad (16)
$$

irrespective of the values of its parameters.

For an observed distribution, the second and fourth moments can be estimated using Eq. (9) and a similar equation for the first moment. The estimated values of the parameters are then given by analogs of Eqs. (12), (13), and (14), namely

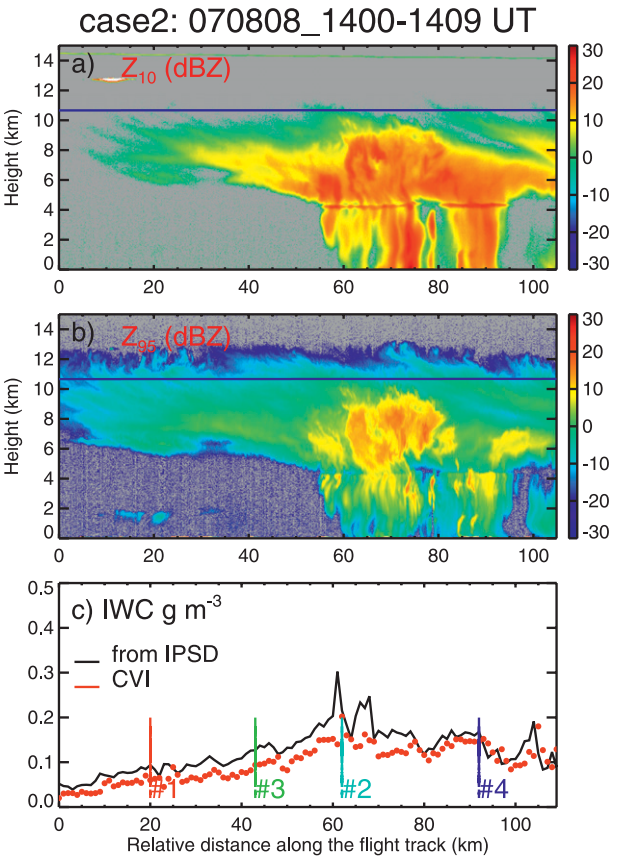

FIG. 4. As in Fig. 2, but for case 2. The vertical lines indicate four selected locations for which IPSDs are plotted in Fig. 5b.

$$ {}^{(G)}\hat{D}_* = \sqrt{\frac{(\hat{M}_2/\hat{M}_1)^2}{16} + \frac{(\hat{M}_4/\hat{M}_2)}{2}} - \left(\frac{3}{4}\right)\left(\frac{\hat{M}_2}{\hat{M}_1}\right), \tag{17} $$

$$ \hat{\mu} = \frac{\hat{M}_2}{\hat{M}_1}\frac{1}{{}^{(G)}\hat{D}_*} - 2, \quad \text{and} \tag{18} $$

$$ {}^{(G)}\hat{N}_0 = \frac{[\hat{M}_1/({}^{(G)}\hat{D}_*^{(\hat{\mu}+2)})]}{\Gamma(\hat{\mu}+2)}. \tag{19} $$

If we now use $y = N_D/({}^{(G)}\hat{N}_0 D^{\hat{\mu}})$ as the transformed concentration density and $x = D/{}^{(G)}\hat{D}_*$ as the size variable, a PSD conforming to the gamma function should tend to collapse onto the exponential curve $y = \exp(-x)$, irrespective of the values of its parameters.

3) LOGNORMAL DISTRIBUTION

For the lognormal distribution, we can use ${}^{(L)}N_D Ds/N_T$ and $\ln(D/{}^{(L)}D_*)/s$ as the transformed concentration and diameter variables. The parameters of the distribution can be expressed in terms of three of its moments. The nth moment is given by

$$ {}^{(L)}M_n = \int_0^\infty D^n({}^{(L)}N_D)\,dD = N_T({}^{(L)}D_*)^n \exp\left(\frac{n^2 s^2}{2}\right). \tag{20} $$

It is noteworthy that the moments consist of three factors and each factor involves only one parameter of the distribution. This is in contrast to the gamma distribution in which the parameters ${}^{(G)}\Lambda$ and μ are entangled [see Eq. (11)].

Using the first, second, and fourth moments, we get

$$ {}^{(L)}D_* = \frac{({}^{(L)}M_2/{}^{(L)}M_1)^2}{\sqrt{{}^{(L)}M_4/{}^{(L)}M_2}}, \tag{21} $$

$$ s = \sqrt{\ln\left[\frac{({}^{(L)}M_4/{}^{(L)}M_1)^{1/3}}{({}^{(L)}M_2/{}^{(L)}M_1)}\right]}, \quad \text{and} \tag{22} $$

$$ N_T = {}^{(L)}M_1\frac{({}^{(L)}M_4/{}^{(L)}M_1)^{1/3}}{({}^{(L)}M_2/{}^{(L)}M_1)^2}. \tag{23} $$

Using the transformed concentration density and size variables, namely

$$ y = \frac{sD^{(L)}N_D}{N_T}, \quad x = \frac{\ln(D/{}^{(L)}D_*)}{s}, \tag{24} $$

any lognormal distribution takes on the standard Gaussian form:

$$ y = \left(\frac{1}{\sqrt{2\pi}}\right)\exp\left(-\frac{x^2}{2}\right). \tag{25} $$

For an observed distribution the moments can be estimated as before. Estimates of the parameters of its lognormal representation are obtained by replacing the analytical moments on the right-hand sides of (21), (22), and (23) by their estimated values:

$$ {}^{(L)}\hat{D}_* = \frac{(\hat{M}_2/\hat{M}_1)^2}{\sqrt{\hat{M}_2/\hat{M}_2}}, \tag{26} $$

$$ \hat{s} = \sqrt{\ln\left[\frac{(\hat{M}_4/\hat{M}_1)^{1/3}}{(\hat{M}_2/\hat{M}_1)}\right]}, \quad \text{and} \tag{27} $$

$$ \hat{N}_T = \hat{M}_1\frac{(\hat{M}_4/\hat{M}_1)^{1/3}}{(\hat{M}_2/\hat{M}_1)^2}. \tag{28} $$

Using $\hat{s}DN_D/\hat{N}_T$ and $\ln(D/^{(G)}\hat{D}_*)/\hat{s}$ as the transformed concentration and size variables, any lognormal distribution should collapse onto the standard Gaussian curve.

In all three cases, the estimated parameters differ from their analytical or "true" values, even if the measured distribution is sampled from a population that is exactly exponential, gamma, or lognormal, because of 1) instrumental problems, 2) sampling fluctuations, 3) replacement of integrals by summations, and 4) truncation of the distribution. Truncation error refers to the fact that the analytical moments involve integrals extending from zero to infinite diameter, whereas the estimated moments involve finite minimum and maximum diameters. A method of accounting for truncation will be discussed in section 4c.

4. Observed ice particle size distributions: Results

a. Selected size distributions

A total of 189 and 99 size spectra were observed in cases 1 and 2, respectively, giving a grand total of 288 spectra. Figure 5 shows four individual spectra for cases 1 (Fig. 5a) and 2 (Fig. 5b). The vertical lines in Figs. 2c and 4c show the locations of these spectra. Reference to Figs. 2a and 2c shows that the IWC decreases with distance away from the convective core. A comparison of Figs. 5a and 2c shows that particle concentration and size also decrease with distance away from the core. These variations can be attributed to fallout and size sorting in the anvil outflow. In case 2, the samples are somewhat symmetrically distributed with respect to the convective core (see Fig. 4a) and consequently particle sorting is not obvious. However, the IWC is seen to decrease with distance on either side of the convective core (Fig. 4c).

We see that spectra with a higher IWC extend to larger sizes and are less steep than spectra with a lower IWC. In both cases, the spectra are approximately exponential, especially at the lower values of the IWC, and tend to have a common intercept on the ordinate. In this respect the spectra are reminiscent of the Marshall–Palmer distribution of raindrop sizes (Marshall and Palmer 1948). However, unlike the Marshall–Palmer distribution, these spectra exhibit a distinct curvature, which becomes more pronounced as the IWC increases.

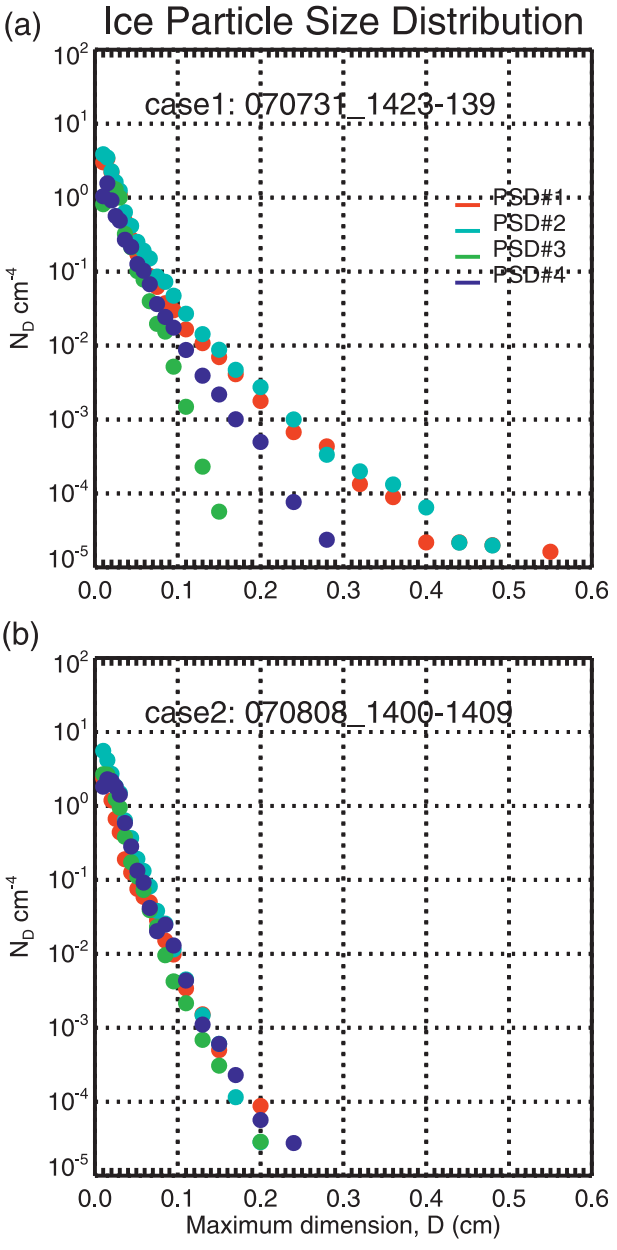

FIG. 5. Four selected IPSDs for cases (a) 1 and (b) 2. The vertical lines in Figs. 2c and 4c show the locations of these IPSDs.

b. Transformed size distributions

We now apply the transformations presented in section 3b to find which function—exponential, gamma, or lognormal—best fits the data. Figures 6a and 6b show the IPSDs for cases 1 and 2 with transformed concentration and diameter axes, $N_D/^{(E)}\hat{N}_0$ and $D/^{(E)}\hat{D}_*$ [Eqs. (6), (7), and (8)], appropriate for the exponential function (Figs. 6c and 6d will be discussed later). Since the observed spectra do not collapse onto the theoretical curve (shown by the solid lines) and moreover show systematic departures from it, we may conclude that the exponential function is not a good fit for the observed spectra.

Figures 7a and 7b (Figs. 7c and 7d will be discussed later) show scatterplots of all the spectra for cases 1 and 2

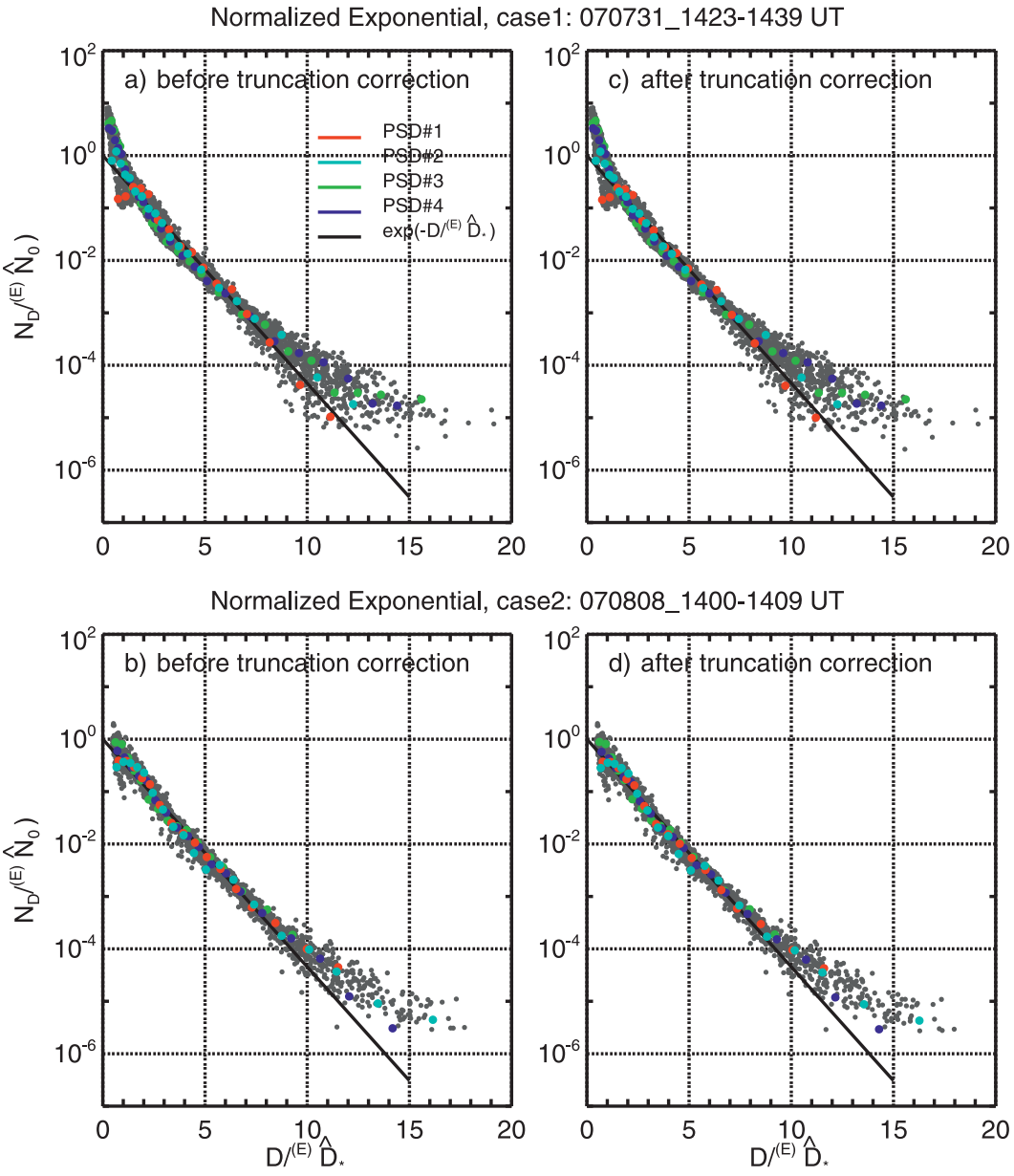

FIG. 6. Observed distributions in transformed coordinates for all IPSDs along the flight line for cases (a),(c) 1 and (b),(d) 2, both (a),(b) before and (c),(d) after truncation correction. Any exponential distribution should collapse onto the black solid line. (See text for details.)

using $D/^{(G)}\hat{D}_*$ and $N_D/(^{(G)}\hat{N}_0 D^{\hat{\mu}})$ as the transformed particle size and concentration variables. If the observed distributions obey the gamma function, then the plotted points should collapse onto the exponential curve shown by the solid line. The gamma function provides a fairly good fit, in the midrange of scaled particle sizes, between about $D/\hat{D}_* = 1$ and 8. The fit is not good for smaller and larger sizes, especially the larger sizes, where the observed points depart systematically from the expected curve. It may be noted that about 10% of all the points plotted satisfy $D/\hat{D}_* < 1$. Of these about 30% lie in the smallest size category, 0.01–0.015 cm, falling progressively to less than 2% for the size category 0.036–0.044 cm. Particles with sizes larger than 0.044 cm have $D/\hat{D}_* \geq 1$.

Figures 8a and 8b (Figs. 8c and 8d will be discussed later) show scatterplots of all the spectra for cases 1 and 2 using $\ln(D/^{(L)}\hat{D}_*)/\hat{s}$ and $\hat{s}DN_D/\hat{N}_T$ as the transformed particle size and concentration variables. The solid lines show the expected curves for the lognormal distribution.

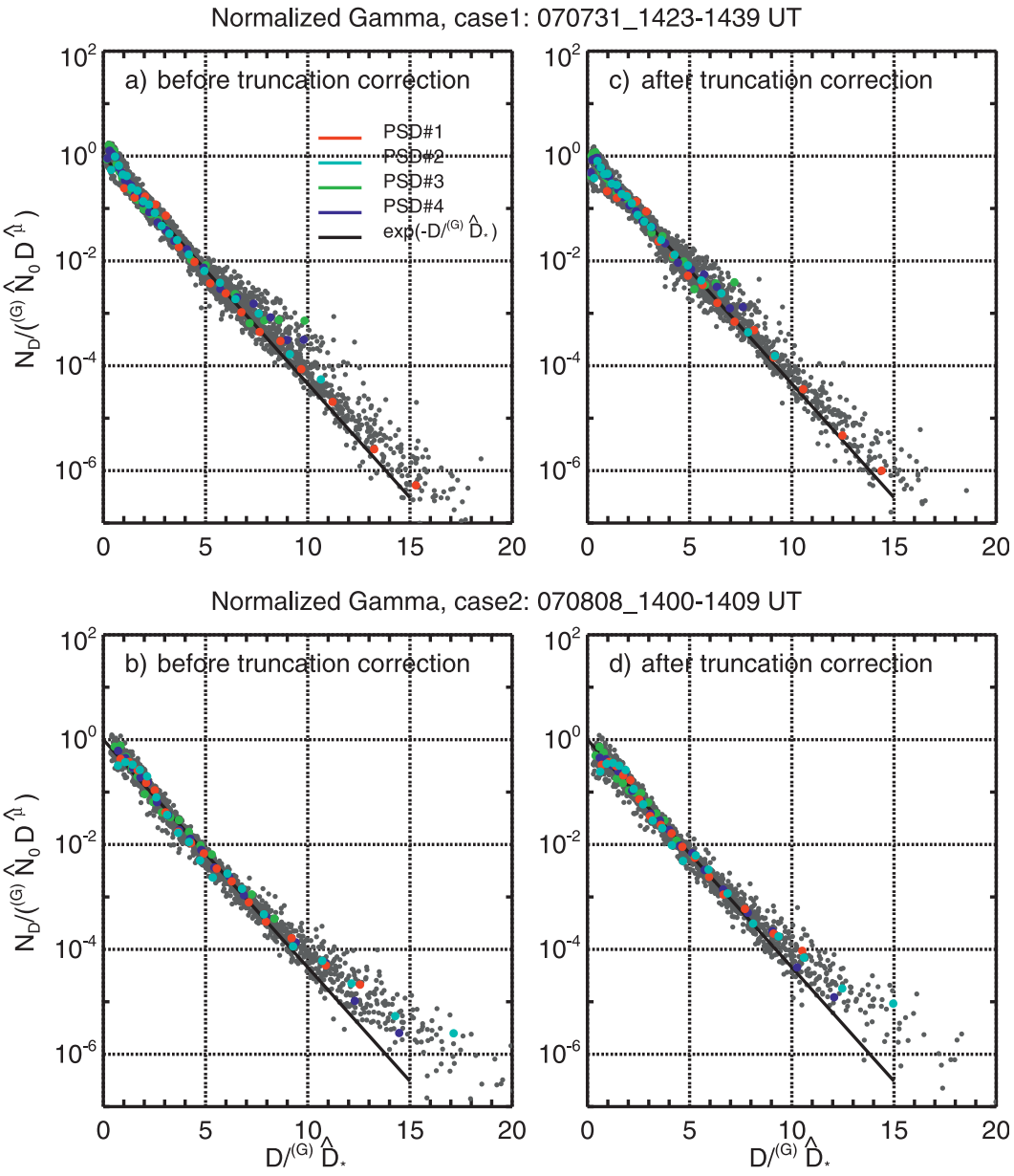

FIG. 7. As Fig. 6, but for the gamma distribution.

We see that the points scatter rather tightly around the theoretical curve. A careful examination of the figures reveals that the fit is better in the midsize range, the scatter being greater at larger and smaller sizes. The greater scatter at larger sizes is to be expected (in all three cases) because of sampling fluctuations. Furthermore, we notice that in both cases the points tend to be a little below the theoretical curve for normalized sizes in the range of about 1 to 2 and a little above it in the range 2 to 4. Some of these systematic deviations disappear after correction for truncation (see section 4c below).

Figures 6–8 suggest that the lognormal function provides a better fit to the observed particle size distributions. The exponential and gamma functions provide a good fit at small and medium sizes but underestimate the concentration at larger sizes. The function fits are discussed further in section 4d.

c. *Truncation correction*

1) EQUATIONS

The equations derived in section 3b assume that the size distributions extend from zero to infinite particle

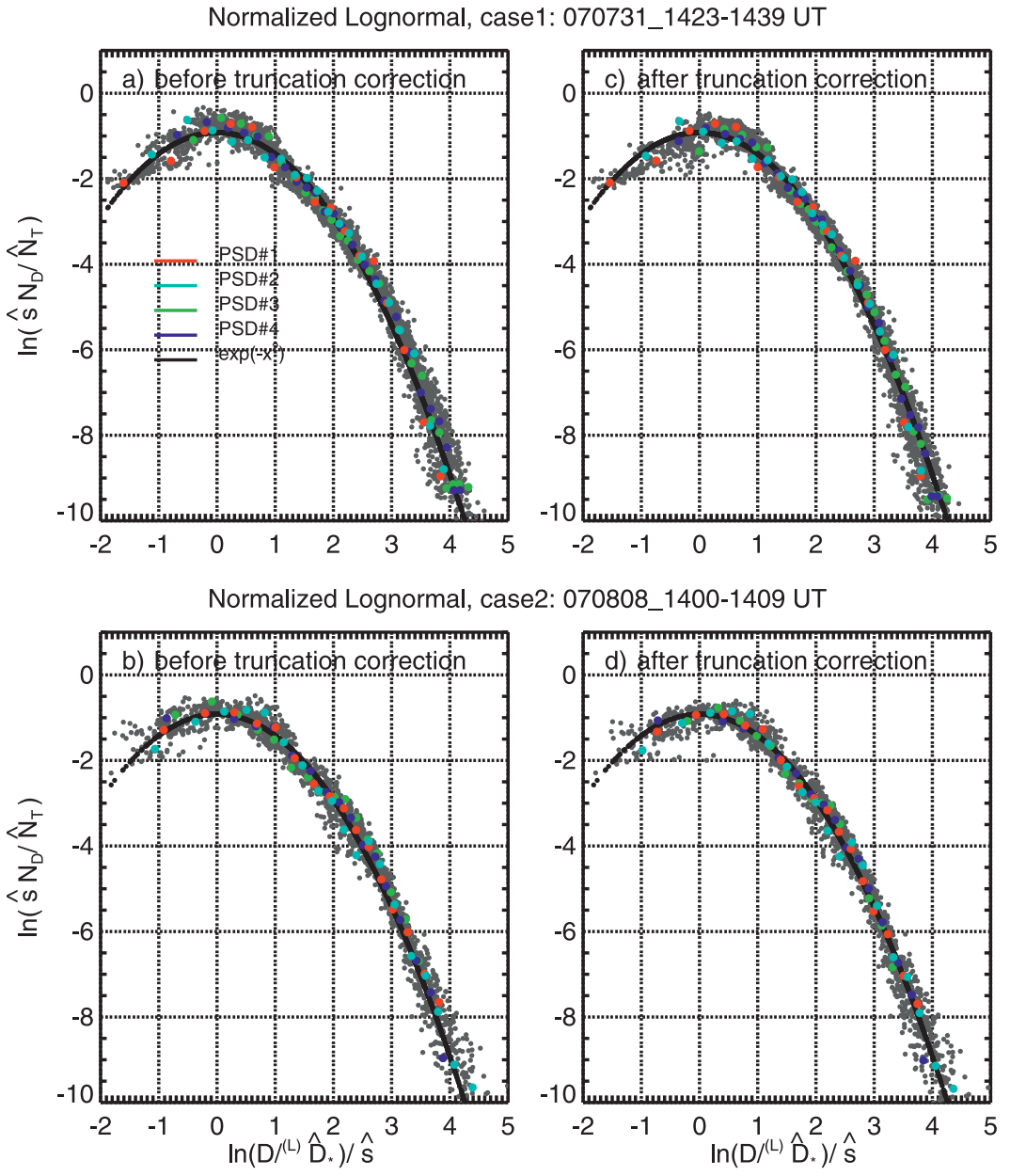

FIG. 8. As Fig. 6, but for the lognormal distribution. Any lognormal distribution should collapse onto the black solid line $\exp(-x^2)$, with $x = \ln(D/{}^{(L)}D_*)/s$.

sizes. The observed distributions extend only from a minimum nonzero diameter $D_{\min}$ to a finite maximum diameter $D_{\max}$. We now present a method for determining the parameters of the three distributions taking account of this truncation.

For the exponential function, we derived the uncorrected distribution parameters by solving Eqs. (4) and (5), which relate the distribution parameters to the untruncated moments. To find the truncation-corrected parameters, we need to relate the parameters to the truncated moments. The nth truncated moment of the exponential distribution is given by

$$
\begin{aligned}
{}^{(E)}M_n(D_{\min}, D_{\max}) &= \int_{D_{\min}}^{D_{\max}} {}^{(E)}N_D D^n \, dD \\
&= \frac{{}^{(E)}N_0}{{}^{(E)}\Lambda^{n+1}} [\gamma(n+1, x_{\max}) \\
&\quad - \gamma(n+1, x_{\min})], \qquad (29)
\end{aligned}
$$

where

$$x_{\min} = {}^{(E)}\Lambda D_{\min} = \frac{D_{\min}}{{}^{(E)}D_*},$$
$$x_{\max} = {}^{(E)}\Lambda D_{\max} = \frac{D_{\max}}{{}^{(E)}D_*}, \quad (30)$$

and γ is the incomplete gamma function. Equation (29) may be rewritten as

$${}^{(E)}M_n(0, \infty) = \frac{\hat{M}_n}{\rho(n+1, x_{\max}) - \rho(n+1, x_{\min})}, \quad (31)$$

where ρ represents the ratio of the incomplete to the complete gamma functions and we have replaced the truncated moment, ${}^{(E)}M_n(D_{\min}, D_{\max})$, by the observed moment $\hat{M}_n$. To obtain the corrected distribution parameters, we need to solve Eq. (31) for $n = 2, 4$. The solution is obtained by an iterative procedure. First, the previously calculated uncorrected parameters and the observed values of $D_{\min}$ and $D_{\max}$ are used to calculate $x_{\min}$ and $x_{\max}$ [Eq. (30)], which are then substituted in Eq. (31) to obtain a first approximation to the untruncated moments, ${}^{(E)}M_n(0, \infty), n = 2, 4$. These are used in Eq. (10) to calculate the first approximation to the corrected parameters, which are in turn used to obtain the next approximations to $x_{\min}$, $x_{\max}$, ${}^{(E)}M_n(0, \infty)$, and the distribution parameters. The procedure is repeated until successive approximations to the distribution parameters differ by less than a set criterion, usually 0.01%. This procedure converges rapidly. Usually no more than 10 iterations are needed. For the gamma function, the procedure is similar to that for the exponential distribution. By considering the truncated moments for the gamma function, we obtain an equation similar to Eq. (31),

$${}^{(G)}M_n(0, \infty) = \frac{\hat{M}_n}{\rho(n+\mu+1, y_{\max}) - \rho(n+\mu+1, y_{\min})}, \quad (32)$$

where

$$y_{\min} = {}^{(G)}\Lambda D_{\min} = \frac{D_{\min}}{{}^{(G)}D_*},$$
$$y_{\max} = {}^{(G)}\Lambda D_{\max} = \frac{D_{\max}}{{}^{(G)}D_*}. \quad (33)$$

Equation (32) is solved iteratively for $n = 1, 2, 4$ to find the truncation-corrected values of the distribution parameters ${}^{(G)}N_0$, ${}^{(G)}D_* = 1/{}^{(G)}\Lambda$, and μ. Again, the convergence is rapid except for negative value of μ close to -2. This is because the first moment, ${}^{(G)}M_1(0, \infty)$, does not exist for $\mu \le -2$. It may be mentioned that an absolute rather than a relative convergence criterion is used for μ. Convergence is considered achieved when successive approximations to μ differ by less than 0.01. This is necessary because μ can be close to zero.

For the lognormal distribution, the nth truncated moment is given by

$${}^{(L)}M_n(D_{\min}, D_{\max}) = \frac{{}^{(L)}M_n(0, \infty)[\mathrm{erf}(z_{\max}) - \mathrm{erf}(z_{\min})]}{2}, \quad (34)$$

where

$$z_{\min} = \frac{[\ln(D_{\min}/{}^{(L)}D_*)/s - ns]}{\sqrt{2}},$$
$$z_{\max} = \frac{[\ln(D_{\max}/{}^{(L)}D_*)/s - ns]}{\sqrt{2}}. \quad (35)$$

Again, we rewrite (34) as

$${}^{(L)}\hat{M}_n(0, \infty) = \frac{2\hat{M}_n}{[\mathrm{erf}(z_{\max}) - \mathrm{erf}(z_{\min})]}. \quad (36)$$

This equation is solved iteratively for $n = 1, 2, 4$ to get truncation-corrected parameters $\hat{N}_T$, $\hat{s}$, and ${}^{(L)}\hat{D}_*$. The convergence is again rapid as in the case of the exponential distribution.

2) Truncation-corrected transformed distributions

A comparison of the distribution parameters, before and after truncation correction, will be presented in the section 4e. Here we compare the transformed distributions before and after truncation correction. The right panels of Figs. 6–8 show scatterplots of the transformed distributions after truncation correction. For the exponential function (Figs. 6c,d), there is very little change after the truncation correction. In the case of the gamma distribution (Figs. 7c,d), there is perhaps a small improvement in the fit to the theoretical curve after the truncation correction. For the lognormal case (Figs. 8c,d), the agreement between the observed spectra and the theoretical curve improves after the truncation correction. Almost all the points at the left-hand side of the plot, which show greater deviations from the theoretical curve, belong to the first size category used in the plots. This size category may not have been sampled properly or may suffer from artifacts of particle shattering at the sensor probe. Of course, it is also possible that the smaller particles do not conform to a lognormal distribution.

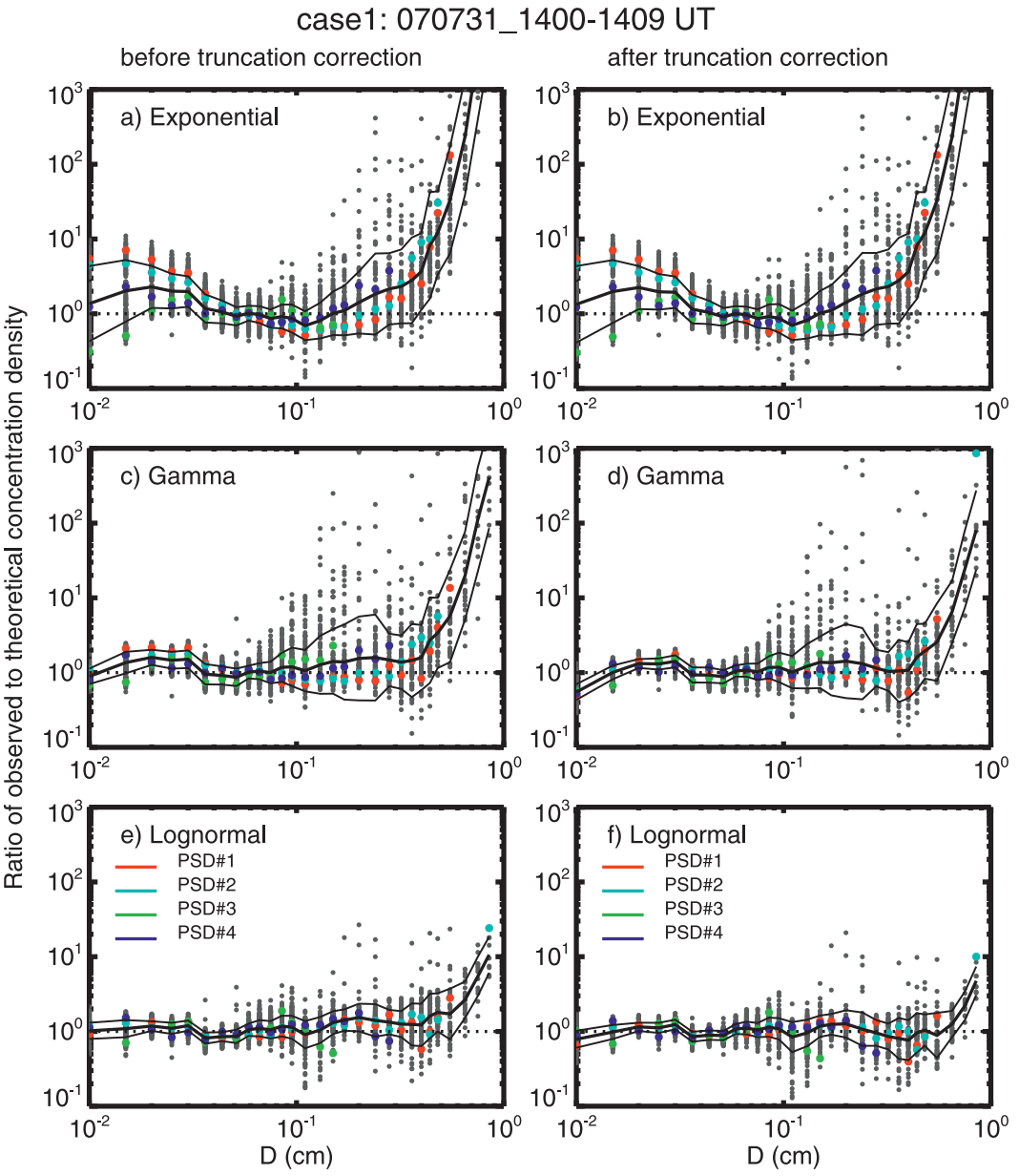

FIG. 9. Ratio of observed to theoretical concentration density as a function of particle diameter for case 1, (left) before and (right) after truncation correction, for (a),(b) exponential, (c),(d) gamma, and (e),(f) lognormal distribution. The solid thick line is the geometric mean and the thin lines are one standard deviation above and below the mean. (For details, see text.)

d. Which function provides a better fit to the observed distributions?

A visual inspection of Figs. 6–8 shows that the lognormal function provides a better fit to the data. The observed IPSD departs from the exponential and gamma functions at the small and large size ends, and there is considerable scatter in the data points. At the large size end, the deviations occur systematically in one direction, the observed concentrations being generally greater than expected. This is true to a smaller extent at the small size end as well. In the case of the lognormal distribution, on the other hand, the observed points scatter tightly around the theoretical curve.

To quantify the above visual impressions, we present the ratios of the observed to expected concentrations in Fig. 9 for case 1 and Fig. 10 for case 2. The expected concentrations were computed for each observed spectrum

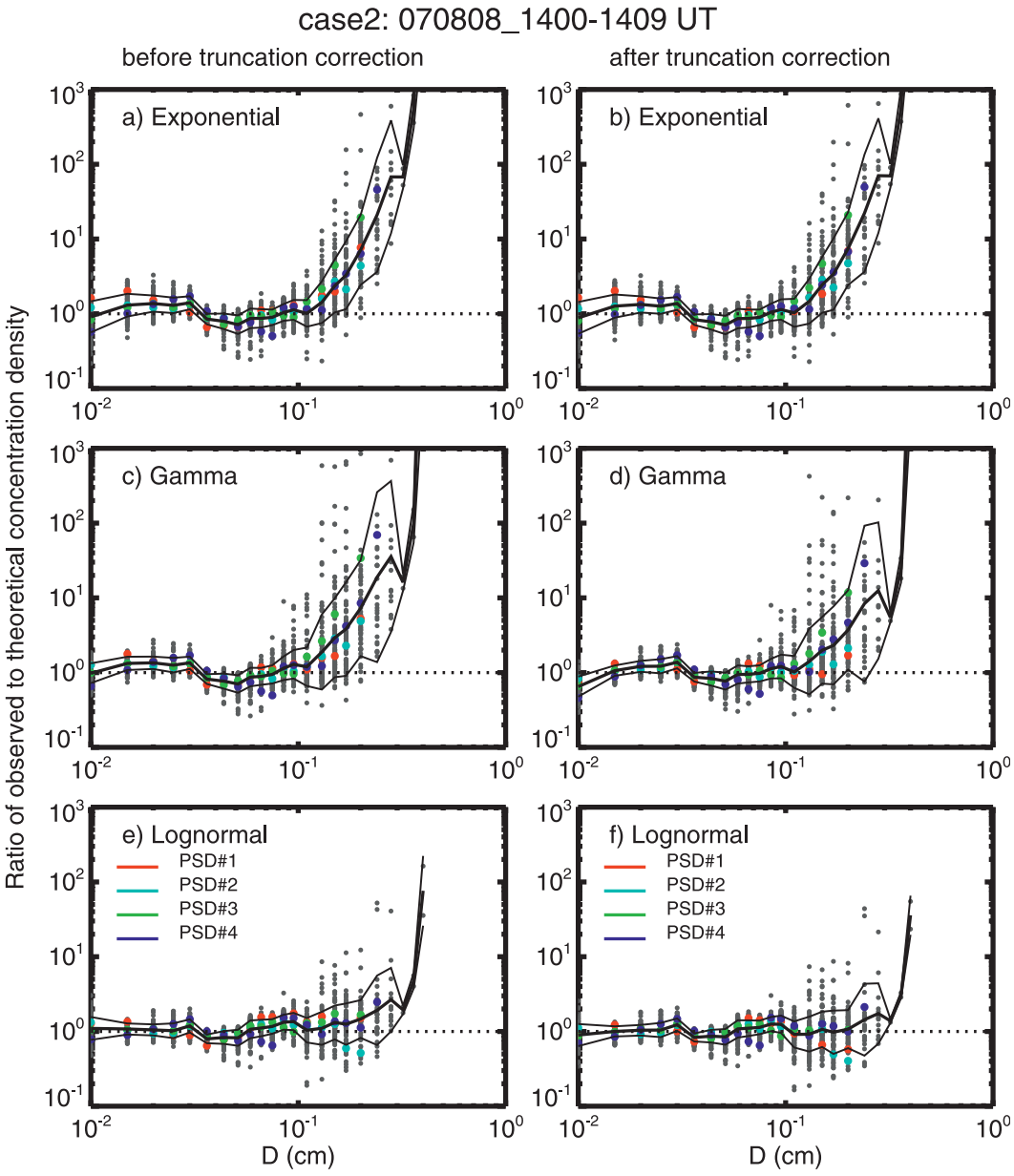

FIG. 10. As in Fig. 9, but for case 2.

using the estimated parameters for that spectrum before (left panels) and after (right panels) truncation correction. In addition, the mean and standard deviations of the logarithms of the ratios were computed as a function of particle size. The logarithms were used because the ratio spans more than four orders of magnitude. The full lines show the mean ratios and points differing from the mean by ±one standard deviation.

In case 1, the observations do not fit the exponential function well (Figs. 9a,b), the mean ratio being greater than 1 for all but a small range of midsized particles. At the large size end, the observed concentrations exceed the theoretical concentrations by orders of magnitude. Truncation correction does not improve the situation (Fig. 9b). In case 2 (Figs. 10a,b) the exponential function also does not provide a good fit to the observations except for diameters less than about 1 mm.

The gamma function provides a somewhat better fit (Figs. 9c,d and 10c,d) than the exponential function. In case 1, without truncation correction, the mean ratios hover around 1 for particle sizes smaller than about 1-mm diameter. For larger sizes, however, the mean ratio exceeds 1 systematically and by a rather wide margin for particles bigger than about 2–3-mm diameter (Fig. 9c).

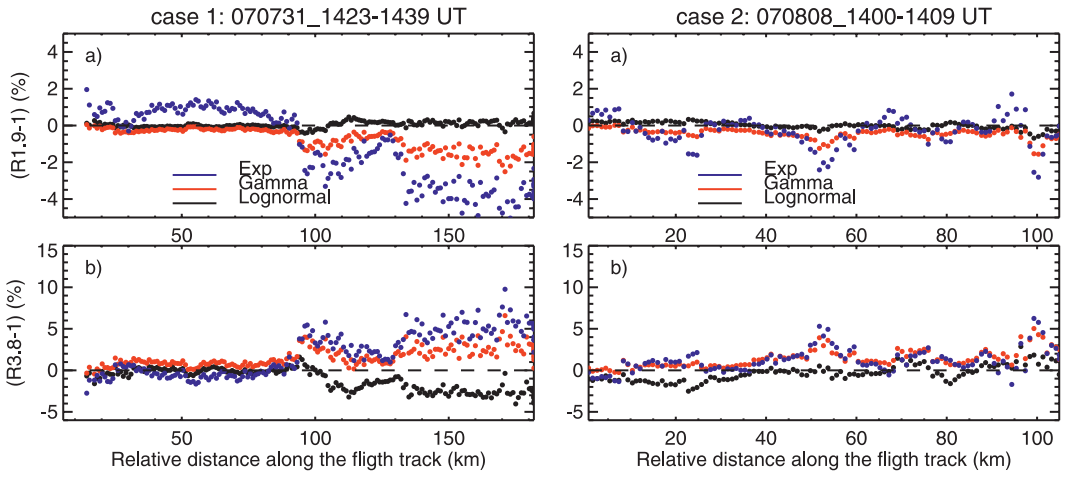

FIG. 11. Percent difference between observed and theoretical 1.9th and 3.8th moments before truncation correction for the exponential (blue), gamma (red), and lognormal (black) fits along the flight track for cases (left) 1 and (right) 2.

Truncation correction improves the fit, with the mean ratio being brought close to 1 for particles up to 4-mm diameter (Fig. 9d). For larger particles, the mean ratio rapidly increases above unity and becomes quite large. In case 2 (Figs. 10c,d), the fit is not as good as in case 1, and truncation correction does not improve the result.

The lognormal function provides a very good fit for case 1 (Fig. 9e). The fit improves after truncation correction (Fig. 9f), with the mean ratio being close to 1 up to a particle diameter of about 6 mm, which is near the limit of the largest particle size measured. The scatter around the mean ratio curve is smaller than in the other cases. The lognormal distribution provides a good fit for case 2 also (Fig. 10e). Truncation correction (Fig. 10f) again improves the fit but not as much as in case 1.

The above tests tell us how well the three functions represent the observed concentration densities. In many cases, however, the moments of the distribution are of greater interest. For example, we might be interested in the ice water content, which is proportional to the 1.9th moment, or the radar reflectivity, which is proportional to 3.8th moment, for Rayleigh scattering, assuming the Brown and Francis (1995) mass–diameter relationship. To test how well the three functions reproduce these moments, we have calculated the following ratios:

$$R_{nE} = \frac{\hat{M}_n}{{}^{(E)}\hat{M}_n}, \quad R_{nG} = \frac{\hat{M}_n}{{}^{(G)}\hat{M}_n},$$

$$R_{nL} = \frac{\hat{M}_n}{{}^{(L)}\hat{M}_n}, \quad n = 1.9,\ 3.8. \tag{37}$$

The numerators, $\hat{M}_n$, are the observed moments. The denominators are calculated using Eqs. (11) and (20) for

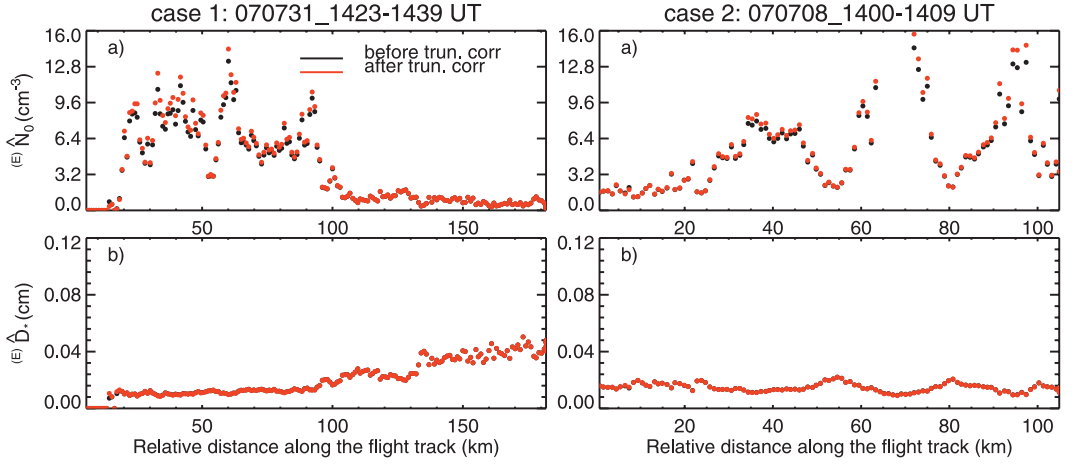

FIG. 12. Parameters (a) ${}^{(E)}\hat{N}_0$ and (b) ${}^{(E)}\hat{D}_*$, for exponential distribution, along the flight track for cases (left) 1 and (right) 2, both before (black) and after (red) truncation correction.

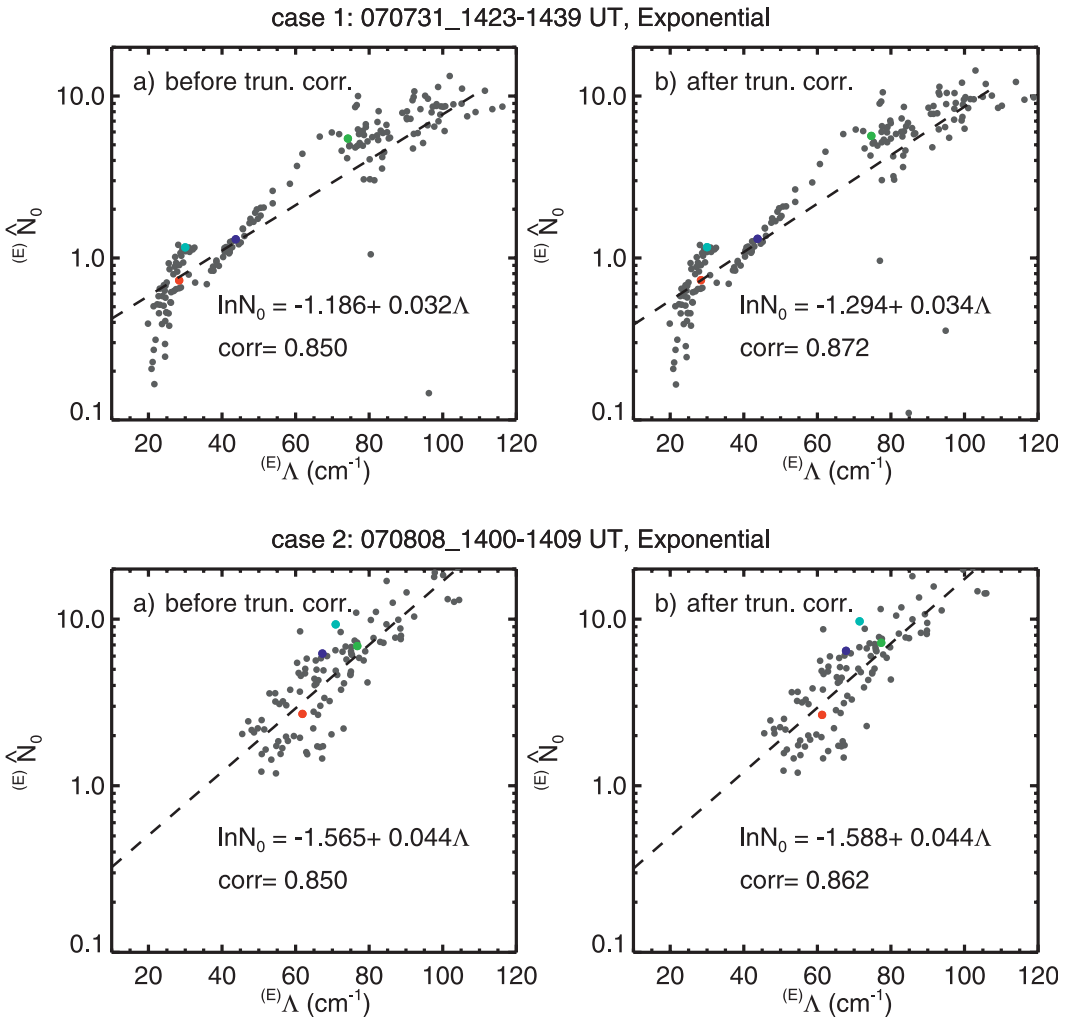

FIG. 13. Scatterplots of $^{(E)}\hat{N}_0$ vs $^{(E)}\Lambda$ (left) before and (right) after truncation correction, for cases (top) 1 and (bottom) 2. Correlation coefficients (corr.) are displayed.

the gamma and lognormal case and Eq. (11) with $\mu = 0$ for the exponential case.

Figure 11 shows the percentage deviations from unity of the ratios for the 1.9th and 3.8th moments, for cases 1 and 2 respectively, plotted along the flight tracks. Note the change in the ordinate scales between the plots for the two moments. In case 1 (left panel), the computed 1.9th moments agree with the observed moments to within 4% for all three functional representations, although in case 1, the exponential and gamma functions show a systematic derivation from unity for the 1.9th moment. The 3.8th moments also agree to within 5% for all three functions. The small disagreements appear for the higher ice water contents. In case 2 (right panel), both moments show excellent agreement between observed and computed moments for all three functions. We see that the percentage deviations are somewhat larger and more erratic for the gamma function. However, for both moments and all three functions, the percentage deviations are rather small. This excellent agreement is not surprising since the parameters of the distributions were derived using the first, second, and fourth moments calculated from the IPSDs. Indeed, a comparison of calculated and observed moments, of orders close to those used to estimate the distribution parameters in the first place, does not constitute a sensitive test of the closeness of the fitted distribution to the observations. A similar calculation of the ratios using the truncation-corrected distribution parameters (figure not shown) gave similar results.

e. *Parameters of the distributions*

In this section, we discuss the variation of the distribution parameters along the flight tracks and correlations between them. Figures 12a and 12b show $^{(E)}\hat{N}_0$ and $^{(E)}\hat{D}_*$

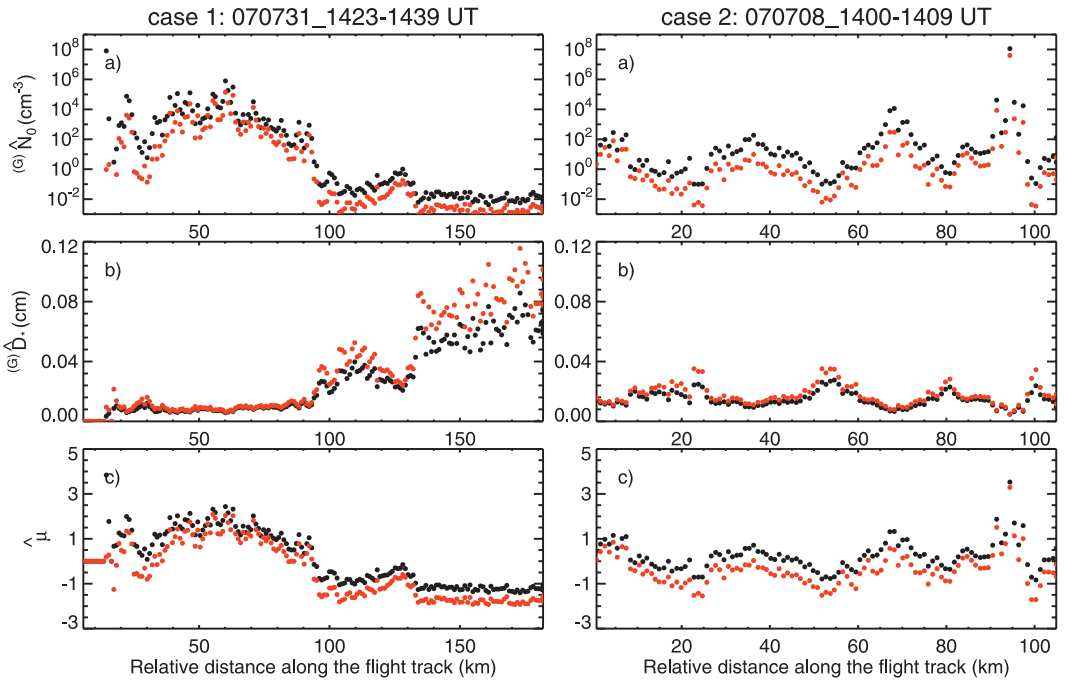

FIG. 14. Parameters (a) ${}^{(G)}\hat{N}_0$, (b) ${}^{(G)}\hat{D}_*$, and (c) $\hat{\mu}$ for gamma distribution for cases (left) 1 and (right) 2.

for case 1 (left panel) and case 2 (right panel) before (black) and after (red) truncation correction. Truncation correction produces only small changes in ${}^{(E)}\hat{N}_0$ and little or no change in ${}^{(E)}\hat{D}_*$. Comparison with a plot of IWC along the flight track for case 1 (Fig. 2c) shows that the IWC and the parameters are correlated, with higher values of ${}^{(E)}\hat{N}_0$ and lower values of ${}^{(E)}\hat{D}_*$ being associated with smaller IWC. Figure 12 also indicates a correlation between ${}^{(E)}\hat{N}_0$ and ${}^{(E)}\hat{\Lambda}_0$ $(=1/{}^{(E)}\hat{D}_*)$. This is confirmed by a scatterplot of ${}^{(E)}\hat{N}_0$ versus ${}^{(E)}\hat{\Lambda}_0$ (Figs. 13a,b), which shows an exponential relationship between the two parameters. In case 1 (Fig. 13, top panel), we see a "saturation" in the value of ${}^{(E)}\hat{\Lambda}_0$ at about 20 cm^{-1}. Lo and Passarelli (1982) found saturation at about 10–12 cm^{-1} at temperatures warmer compared to our case. Case 2 (Fig. 13, bottom) does not show saturation. This may be because the slope does not fall below about 40 cm^{-1}.

Figures 14a–c show a plot of the parameters of the gamma distribution along the flight track for case 1 (left panel). Comparison with Fig. 4c shows a correlation with the IWC with lower values of IWC being associated with higher ${}^{(G)}\hat{N}_0$ and lower μ. However, a similar plot for case 2 (Fig. 14, right panel) does not show a strong correlation with IWC. Both cases 1 and 2 suggest that the parameters are correlated with each other. This is confirmed by the scatterplots in Fig. 15 (case 1) and Fig. 16 (case 2). The correlation between ${}^{(G)}\hat{N}_0$ and $\hat{\mu}$ is almost perfect in both cases (Figs. 15a,b and 16a,b), with ${}^{(G)}\hat{N}_0$ being an exponential function of μ. Ulbrich (1983) reported a similar relationship for raindrop size distributions. There is a weaker linear relationship between ${}^{(G)}\hat{\Lambda}$ and μ (Figs. 15c,d and 16c,d). Brandes et al. (2003) have reported a quadratic relationship between ${}^{(G)}\hat{\Lambda}$ and μ for raindrop size distributions.

The parameters of the lognormal distribution are shown in Fig. 17 for case 1 (left) and 2 (right). Comparison with IWC along the flight track (Figs. 2c and 4c) suggests a positive correlation between $\hat{N}_T$ and IWC and a weaker positive correlation between $\hat{s}$ and IWC. Pairwise scatterplots for the three parameters are shown in Fig. 18 (case 1) and Fig. 19 (case 2). There is a fair negative correlation between $\hat{N}_T$ and ${}^{(L)}\hat{D}_*$ in both cases (Figs. 18a,b and 19a,b). In case 1, the correlation improves after truncation correction. There is a good positive correlation between $\hat{N}_T$ and $\hat{s}$ in case 1 (Figs. 18c,d) but it is weak in case 2 (Figs. 19c,d). The poor correlation in case 2 may be due to the small range of values of $\hat{s}$. There is a fair correlation between ${}^{(L)}D_*$ and $\hat{s}$ in both cases (Figs. 18e and 19e). In both cases, the correlation improves rather markedly after truncation correction (Figs. 18f and 19f).

5. Discussion

a. *Comments on the functional representation of PSDs*

The exponential distribution has two adjustable parameters, whereas the gamma and lognormal distributions

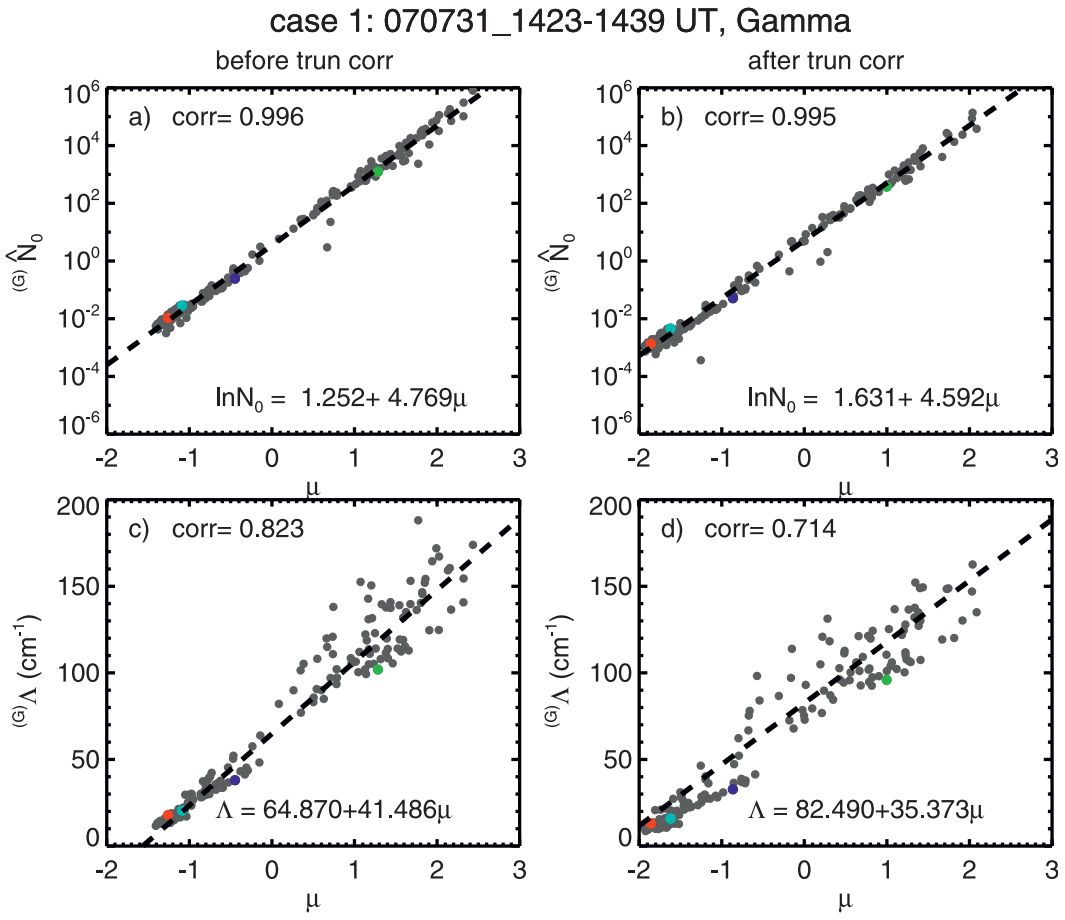

FIG. 15. Scatterplots of ${}^{(G)}\hat{N}_0$ vs $\hat{\mu}$ (top), and ${}^{(G)}\Lambda$ vs $\hat{\mu}$ (bottom), both (left) before and (right) after truncation corrections for case 1. Correlation coefficients (corr.) are displayed.

each have three adjustable parameters. However, the estimates of the parameters of the exponential distribution, ${}^{(L)}\hat{D}_*$ and ${}^{(E)}\hat{N}_0$, are correlated; the estimates of the parameters of the gamma distribution, ${}^{(G)}\hat{D}_*$, $\hat{\mu}$, and ${}^{(G)}\hat{N}_0$, are also correlated in pairs. Therefore, the exponential and gamma distributions have effectively only between one and two *freely* adjustable parameters. The three parameters of the lognormal function show weaker correlations; therefore, the lognormal function has close to three *freely* adjustable parameters.

The parameters of the exponential distribution have the simple interpretation of intercept and slope on a semilogarithmic plot of the PSD. A positive correlation between ${}^{(E)}N_0$ and ${}^{(E)}\Lambda$ is understandable if it is assumed that aggregation is the major factor shaping the size distribution. Then, if we start with an initial exponential distribution, aggregation would tend to increase the concentration of larger particles and decrease that of smaller particles, giving rise to a decrease in both ${}^{(E)}N_0$ and ${}^{(E)}\Lambda$. This tendency can be checked by breakup of larger particles, which may prevent the slope from decreasing below a certain value. Indeed, breakup has sometimes been invoked to explain the observed saturation of ${}^{(E)}\hat{\Lambda}$.

The parameter μ of the gamma distribution can be related to the curvature of the size distribution on a semilogarithmic plot, but the other two parameters do not have a straightforward interpretation. Also, there is no convincing physical explanation of the observed correlations between the parameters of the distribution.

The parameters of the lognormal distribution have a straightforward interpretation: N_T is the total particle concentration, ${}^{(L)}D_*$ is a measure of the ''mean'' particle size, and s is a measure of the spread of the distribution. Indeed, ${}^{(L)}D_* = \exp(\langle \ln D \rangle)$ and $s^2 = \langle \ln^2 D \rangle - \langle \ln D \rangle^2$, where $\langle\ \rangle$ denotes averaging. The transformation of the lognormal distribution also has a simple interpretation. It involves shifting the zero of the size axis to the mean size and scaling it by the standard deviation [$x = \ln(D/{}^{(L)}D_*)/s$], while the normalization of the concentration ($y = sDN_D/N_T$) ensures that the area under the transformed distribution is unity.

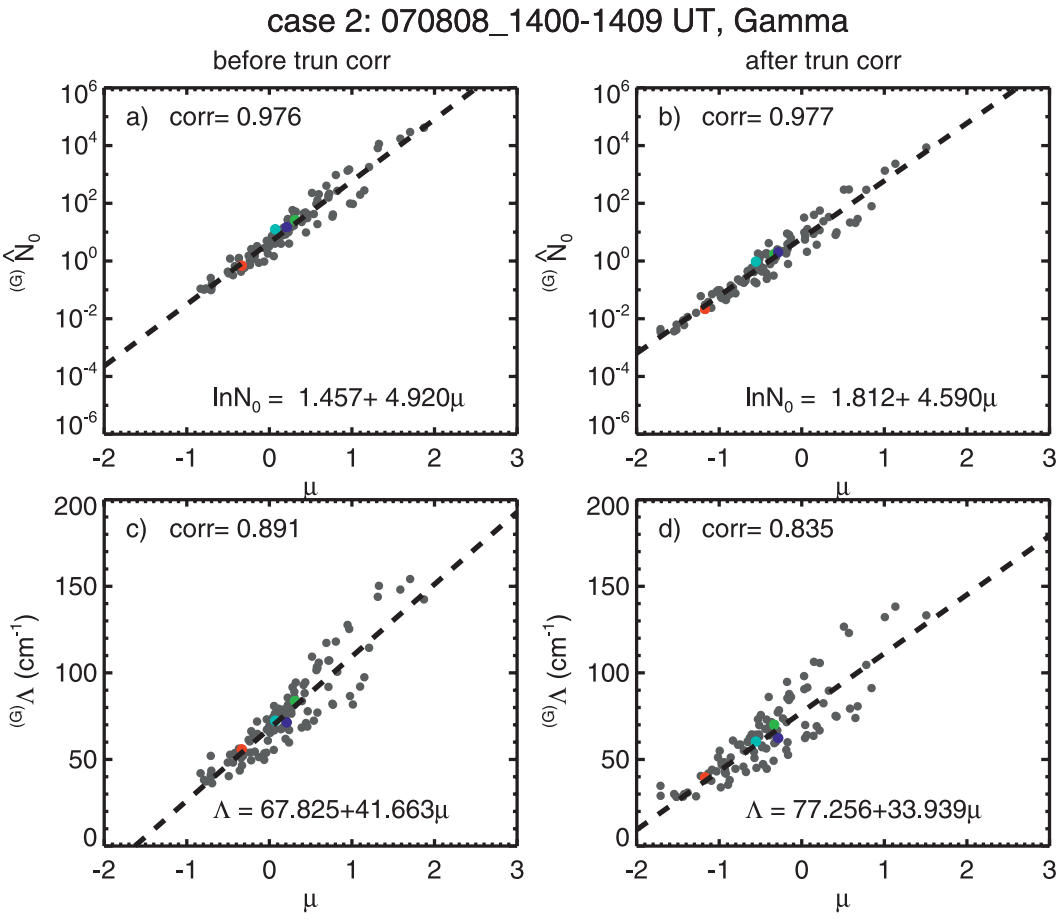

FIG. 16. As in Fig. 15, but for case 2.

b. *Comparison of methods of scaling particle size distributions*

Here we compare our method of transforming particle size distributions with other methods of normalizing the distribution reported in the literature. Many of these methods were initially developed for the analysis of raindrop size distributions (RSDs) and subsequently applied to the analysis of IPSDs. Sekhon and Srivastava (1971) used median volume diameter to scale raindrop diameter and a combination of rainwater content and median volume diameter to scale concentration density. Their scaling collapses the general exponential distribution onto a ''universal'' curve. Testud et al. (2001) used the mean mass diameter, D_m, and a concentration density N_0^* to scale any RSD:

$$\frac{N_D}{N_0^*} = F\left(\frac{D}{D_m}\right). \tag{38}$$

The scaling variables D_m and N_0^* are related to the third and fourth moments of the RSD. With this normalization, two-parameter exponential RSDs collapse onto a universal curve. However, RSDs involving more than two parameters do not collapse onto a single curve. For example, for the gamma function RSD, which involves three parameters, ${}^{(G)}N_0$, Λ, and μ, the normalization eliminates two parameters, ${}^{(G)}N_0$ and Λ, but the function F in Eq. (38) depends on the parameter μ [see Eq. (15) in Testud et al. 2001]. This dependence leads to considerable scatter in plots of RSD using D/D_m and N_D/N_0^* as the normalized diameter and concentration density variables.

Lee et al. (2004) have presented a generalization of the Testud et al. normalization so that any two moments of the RSD can be used to normalize the size and concentration density. Their normalization may be more simply interpreted in terms of nondimensional size and concentration density variables. Consider, for example, the dimensions of the ith and jth moments:

$$[M_i] = [N_D \Delta D][D]^i, \quad [M_j] = [N_D \Delta D][D]^j, \tag{39}$$

where the square brackets denote dimensions. From the above equations, we find the following combinations of

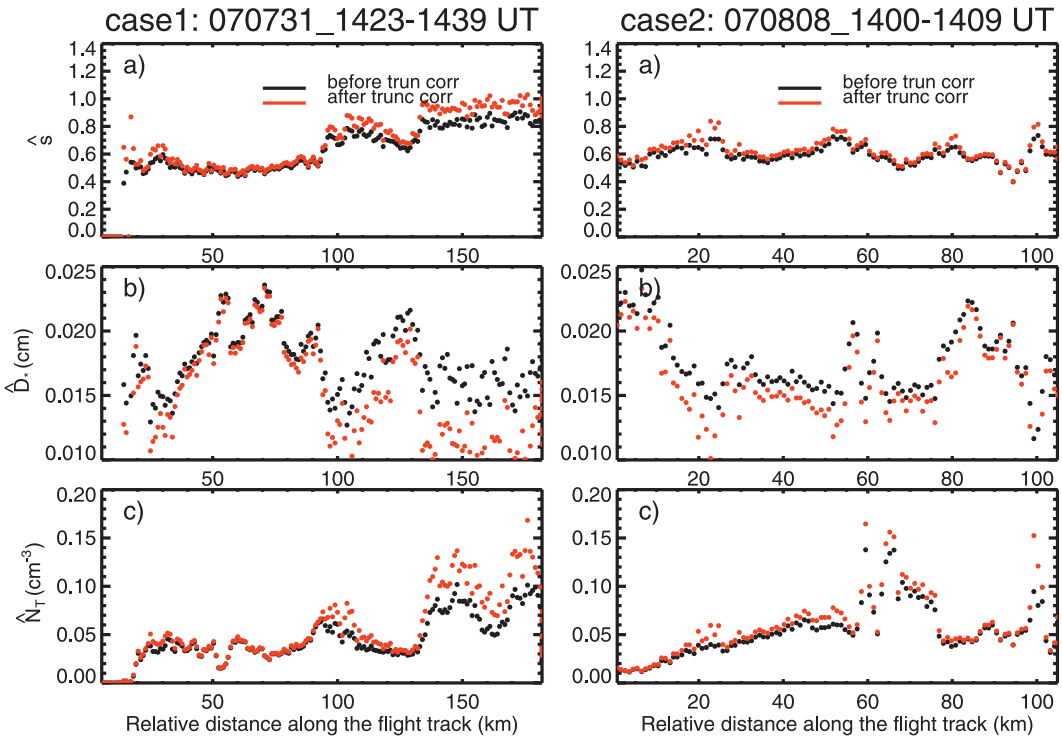

FIG. 17. Parameters $\hat{s}$, ${}^{(L)}\hat{D}_*$, and $\hat{N}_T$ for lognormal distribution along the flight track, both before (black) and after (red) truncation correction, for cases (left) 1 and (right) 2.

moments with dimensions of particle size and concentration density:

$$[D] = \left\{\frac{[M_j]}{[M_i]}\right\}^{1/(j-i)},$$

$$[N_D] = [M_i]^{(j+1)/(j-i)}[M_j]^{-(i+1)/(j-i)}. \quad (40)$$

Thus, we can use the following scales to normalize the diameter and concentration density:

$$D_* = \left(\frac{M_j}{M_i}\right)^{1/(j-i)}, \quad N_* = M_i^{(j+1)/(j-i)} M_j^{-(i+1)/(j-i)}. \quad (41)$$

These are the variables used by Lee et al. to normalize the RSD [see their Eq. (15)]. We can even generalize the above normalization by using two moments to generate a diameter scale and two other moments to generate a concentration density scale.

Field et al. (2005) used the following pairs of moments to scale 9000 observed IPSDs: second and third, second and fourth, and third and fourth (see their Fig. 11). Their normalized spectra show considerable scatter; they do not collapse on to a single curve. Field et al. (2007) used the sum of a gamma and an exponential function to represent their normalized universal distribution. There is a rather large scatter around the universal curve because a two-moment normalization cannot collapse a three-parameter size distributions onto a single curve, and the observed distributions probably require three parameters for a more accurate representation. We have used the second and fourth moments to apply normalization similar to that of Field et al. to our data. The results (not shown) were similar to those of Field et al. The PSD transformations presented here differ from the other normalizations cited above in that they are designed to collapse specific multiparameter particle size distributions to a single curve, whose form is predicted in advance, irrespective of the values of the parameters of the distribution.

6. Summary and conclusions

We have presented methods for transforming exponential, gamma, and lognormal function particle size spectra. In the case of the general exponential distribution with two free parameters, two moments are needed to transform the spectra. We have used the second and fourth moments to derive characteristic size and concentration density scales. We have shown that using these scales, any exponential size distribution can be transformed into a standard exponential distribution

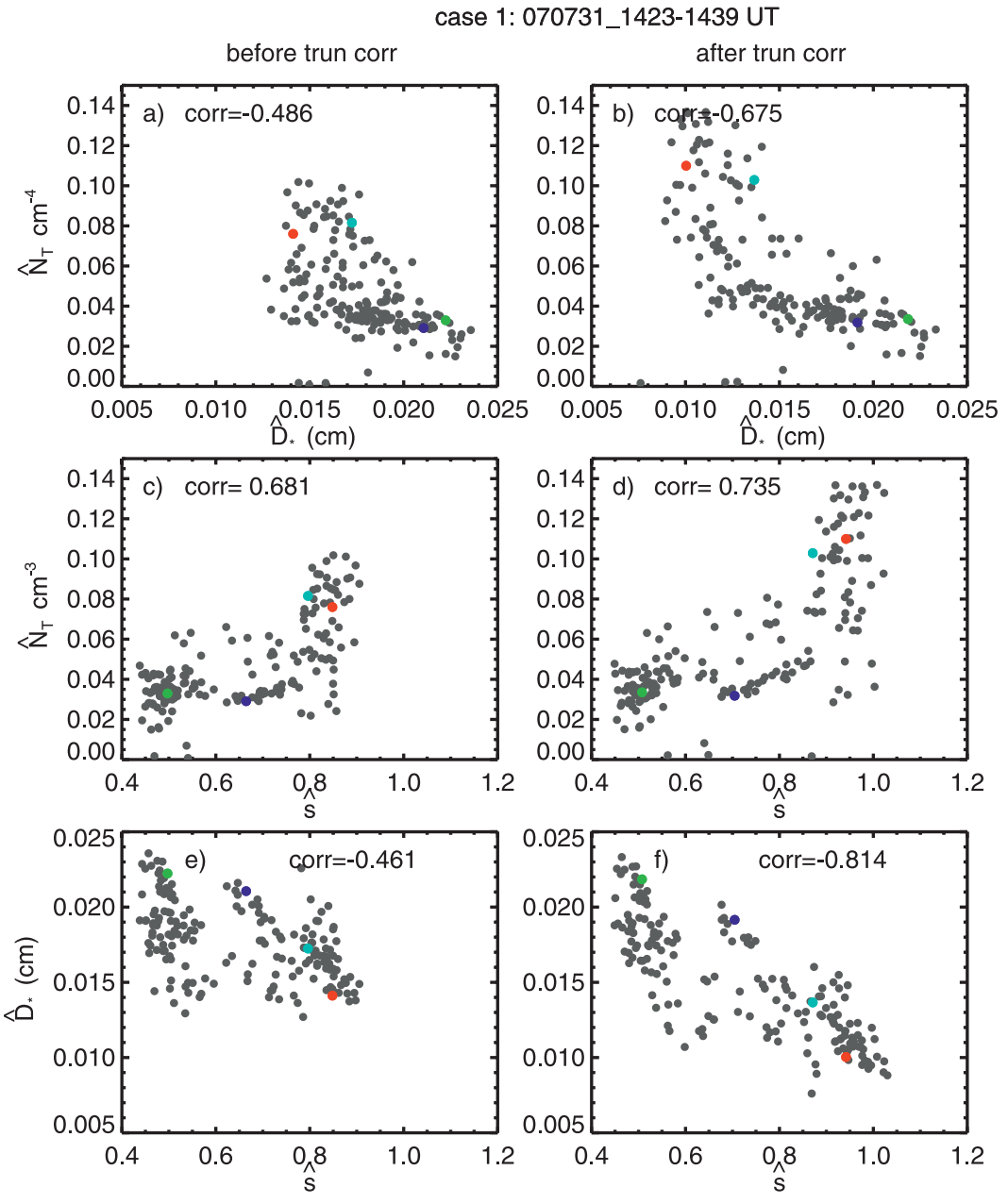

FIG. 18. Scatterplots of (top) $\hat{N}_T$ vs ${}^{(L)}\hat{D}_*$, (middle) $\hat{N}_T$ vs $\hat{s}$, and (bottom) ${}^{(L)}\hat{D}_*$ vs $\hat{s}$, both (left) before and (right) after truncation correction, for case 1. Correlation coefficients (corr.) are displayed.

independent of the values of its parameters. For the gamma and lognormal functions, both of which have three free parameters, we have used three moments to transform the distributions. We have used the first, second, and fourth moments to derive size and concentration density scales for each of the distributions. We have shown that using these scales, the gamma and the lognormal distributions can be transformed to standard exponential and Gaussian forms, respectively, independent of the values of the parameters of the distributions.

We have applied these transformations to two cases of observed ice particle size distributions, in convectively generated cirrus, obtained during the TC4 campaign in Costa Rica. We have found that the observed distributions are not well fitted by the exponential function except in the midsize range of particle sizes; moreover, the observations depart systematically from the expected curve. The gamma function provides a better fit over the midrange and small sizes but underestimates the concentrations at larger sizes. The lognormal function provides

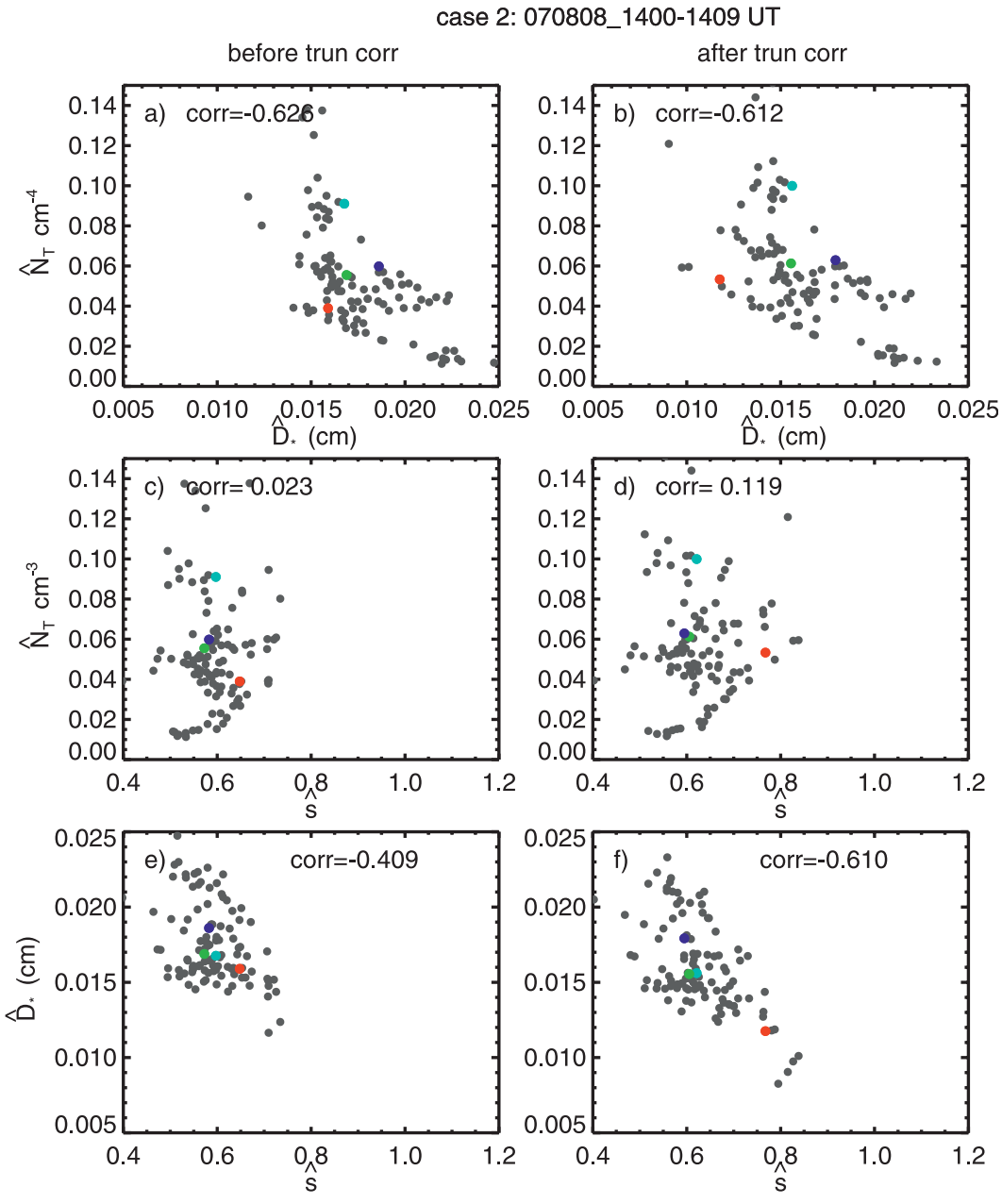

FIG. 19. As in Fig. 18, but for case 2.

the best fit to the data. This conclusion has been supported by an examination of the ratios of observed to theoretically expected concentrations and their means and standard deviations. Our conclusions are based on two cases of observations of ice particles in tropic cirrus. They should be examined using a larger dataset including data from temperate-latitude ice clouds.

Our findings have implications for the remote sensing of ice in clouds. If the three parameters of the lognormal function, used to specify the observed IPSDs, are independent, then it is likely that we will need a minimum of three measurables to remotely sense ice in clouds. We have examined the three parameters for our observations for possible relationships among them and have found that they generally show only fair to weak correlation. We propose to pursue this aspect of the work further by analyzing more extensive datasets on IPSDs including data from temperate-latitude clouds.

Acknowledgments. We thank Ed Zenker and Paul Racette for their engineering support. This work and the radar and in situ data collection were supported by the

TC4 campaign sponsored by the NASA Radiation Sciences Program. Prof. Ramesh Srivastava was supported by a Goddard visiting fellowship at the Goddard Earth Sciences and Technology Center.

REFERENCES

Baumgardner, D., H. Jonsson, W. Dawson, D. O'Connor, and R. Newton, 2002: The cloud, aerosol and precipitation spectrometer: A new instrument for cloud investigations. *Atmos. Res.,* **59–60,** 251–264.

Brandes, E. A., G. Zhang, and J. Vivekanandan, 2003: An evaluation of a drop distribution–based polarimetric radar rainfall estimator. *J. Appl. Meteor.,* **42,** 652–660.

Brown, P. R. A., and P. N. Francis, 1995: Improved measurements of the ice water content in cirrus using a total-water probe. *J. Atmos. Oceanic Technol.,* **12,** 410–414.

Delanoë, J., A. Protat, J. Testud, D. Bouniol, A. J. Heymsfield, A. Bansemer, P. R. A. Brown, and R. M. Forbes, 2005: Statistical properties of the normalized ice particle size distribution. *J. Geophys. Res.,* **110,** D10201, doi:10.1029/2004JD005405.

Feingold, G., and Z. Levin, 1986: The lognormal fit to raindrop spectra from frontal convective clouds in Israel. *J. Appl. Meteor.,* **25,** 1346–1363.

Field, P. R., R. J. Hogan, P. R. A. Brown, A. J. Illingworth, T. W. Choularton, and R. J. Cotton, 2005: Parametrization of ice-particle size distributions for mid-latitude stratiform cloud. *Quart. J. Roy. Meteor. Soc.,* **131,** 1997–2017.

——, A. J. Heymsfield, and A. Bansemer, 2007: Snow size distribution parameterization for midlatitude and tropical ice clouds. *J. Atmos. Sci.,* **64,** 4346–4365.

Gunn, K. L. S., and J. S. Marshall, 1958: The distribution with size of aggregate snowflakes. *J. Atmos. Sci.,* **15,** 452–461.

Heymsfield, A. J., and C. M. R. Platt, 1984: A parameterization of the particle size spectrum of ice clouds in terms of the ambient temperature and the ice water content. *J. Atmos. Sci.,* **41,** 846–855.

——, A. Bansemer, P. R. Field, S. L. Durden, J. L. Stith, J. E. Dye, W. Hall, and C. A. Grainger, 2002: Observations and parameterizations of particle size distributions in deep tropical cirrus and stratiform precipitating clouds: Results from in situ observations in TRMM field campaigns. *J. Atmos. Sci.,* **59,** 3457–3491.

——, ——, C. Schmitt, C. Twohy, and M. R. Poellot, 2004: Effective ice particle densities derived from aircraft data. *J. Atmos. Sci.,* **61,** 982–1003.

Heymsfield, G. M., and Coauthors, 1996: The EDOP radar system on the high-altitude NASA ER-2 aircraft. *J. Atmos. Oceanic Technol.,* **13,** 795–809.

Lee, G., I. Zawadzki, W. Szyrmer, D. Sempere-Torres, and R. Uijlenhoet, 2004: A general approach to double-moment normalization of drop size distributions. *J. Appl. Meteor.,* **43,** 264–281.

Li, L., G. M. Heymsfield, P. E. Racette, L. Tian, and E. Zenker, 2004: A 94-GHz cloud radar system on a NASA high-altitude ER-2 aircraft. *J. Atmos. Oceanic Technol.,* **21,** 1378–1388.

Lo, K. K., and R. E. Passarelli, 1982: The growth of snow in winter storms: An airborne observational study. *J. Atmos. Sci.,* **39,** 697–706.

Locatelli, J. D., and P. V. Hobbs, 1974: Fall speeds and masses of solid precipitation particles. *J. Geophys. Res.,* **79,** 2185–2197.

Marshall, J. S., and W. M. K. Palmer, 1948: The distribution of raindrops with size. *J. Meteor.,* **5,** 165–166.

Seinfeld, J. H., and S. N. Pandis, 1998: *Atmospheric Chemistry and Physics*. John Wiley & Sons, 1326 pp.

Sekhon, R. S., and R. C. Srivastava, 1971: Doppler radar observation of drop size in a thunderstorm. *J. Atmos. Sci.,* **28,** 983–994.

Testud, J., S. Oury, R. A. Black, P. Amayenc, and X. Dou, 2001: The concept of ''normalized'' distribution to describe raindrop spectra: A tool for cloud physics and cloud remote sensing. *J. Appl. Meteor.,* **40,** 1118–1140.

Tinel, C., J. Testud, J. Pelon, R. J. Hogan, A. Protat, J. Delanoë, and D. Bouniol, 2005: The retrieval of ice-cloud properties from cloud radar and lidar synergy. *J. Appl. Meteor.,* **44,** 860–875.

Twohy, C. H., A. J. Schanot, and W. A. Cooper, 1997: Measurement of condensed water content in liquid and ice clouds using an airborne counterflow virtual impactor. *J. Atmos. Oceanic Technol.,* **14,** 197–202.

Ulbrich, C. W., 1983: Natural variations in the analytical form of the raindrop-size distribution. *J. Climate Appl. Meteor.,* **22,** 1764–1775.

Waldvogel, A., 1974: The N_0 jump of raindrop spectra. *J. Atmos. Sci.,* **31,** 1067–1078.

Willis, P. T., 1984: Functional fits to some observed drop size distributions and parameterization of rain. *J. Atmos. Sci.,* **41,** 1648–1661.